Taxodione and arenarone inhibit farnesyl diphosphate synthase by binding to the isopentenyl diphosphate site

Yi-Liang Liu[a,1], Steffen Lindert[b,c,1], Wei Zhu[a], Ke Wang[a], J. Andrew McCammon[b,c,d,e,2], and Eric Oldfield[a,f,2]

[a]Department of Chemistry and [f]Center for Biophysics and Computational Biology, University of Illinois at Urbana–Champaign, Urbana, IL 61801; Departments of [b]Pharmacology and [e]Chemistry and Biochemistry and [d]Howard Hughes Medical Institute, University of California, San Diego, La Jolla, CA 92093; and [c]National Science Foundation Center for Theoretical Biological Physics, La Jolla, CA 92093

Contributed by J. Andrew McCammon, May 16, 2014 (sent for review April 7, 2014; reviewed by Wolfgang Jahnke)

We used in silico methods to screen a library of 1,013 compounds for possible binding to the allosteric site in farnesyl diphosphate synthase (FPPS). Two of the 50 predicted hits had activity against either human FPPS (HsFPPS) or *Trypanosoma brucei* FPPS (TbFPPS), the most active being the quinone methide celastrol (IC_{50} versus TbFPPS ∼20 μM). Two rounds of similarity searching and activity testing then resulted in three leads that were active against HsFPPS with IC_{50} values in the range of ∼1–3 μM (as compared with ∼0.5 μM for the bisphosphonate inhibitor, zoledronate). The three leads were the quinone methides taxodone and taxodione and the quinone arenarone, compounds with known antibacterial and/or antitumor activity. We then obtained X-ray crystal structures of HsFPPS with taxodione+zoledronate, arenarone+zoledronate, and taxodione alone. In the zoledronate-containing structures, taxodione and arenarone bound solely to the homoallylic (isopentenyl diphosphate, IPP) site, not to the allosteric site, whereas zoledronate bound via Mg^{2+} to the same site as seen in other bisphosphonate-containing structures. In the taxodione-alone structure, one taxodione bound to the same site as seen in the taxodione+zoledronate structure, but the second located to a more surface-exposed site. In differential scanning calorimetry experiments, taxodione and arenarone broadened the native-to-unfolded thermal transition (T_m), quite different to the large increases in ΔT_m seen with biphosphonate inhibitors. The results identify new classes of FPPS inhibitors, diterpenoids and sesquiterpenoids, that bind to the IPP site and may be of interest as anticancer and antiinfective drug leads.

prenyl synthase | crystallography | prenylation | molecular dynamics | drug discovery

Farnesyl diphosphate synthase (FPPS) catalyzes the condensation of isopentenyl diphosphate (IPP; compound **1** in Fig. 1) with dimethylallyl diphosphate (DMAPP; compound **2** in Fig. 1) to form the C_{10} isoprenoid geranyl diphosphate (GPP; compound **3** in Fig. 1), which then condenses with a second IPP to form the C_{15} isoprenoid, farnesyl diphosphate (FPP; compound **4** in Fig. 1). FPP then is used in a wide range of reactions including the formation of geranylgeranyl diphosphate (GGPP) (1), squalene (involved in cholesterol and ergosterol biosynthesis), dehydrosqualene (used in formation of the *Staphylococcus aureus* virulence factor staphyloxanthin) (2), undecaprenyl diphosphate (used in bacterial cell wall biosynthesis), and quinone and in heme a/o biosynthesis. FPP and GGPP also are used in protein (e.g., Ras, Rho, Rac) prenylation, and FPPS is an important target for the bisphosphonate class of drugs (used to treat bone resorption diseases) such as zoledronate (compound **5** in Fig. 1) (3). Bisphosphonates targeting FPPS have activity as antiparasitics (4), act as immunomodulators (activating γδ T cells containing the Vγ2Vδ2 T-cell receptor) (5), and switch macrophages from an M2 (tumor-promoting) to an M1 (tumor-killing) phenotype (6). They also kill tumor cells (7) and inhibit angiogenesis (8). However, the bisphosphonates in clinical use (zoledronate, alendronate, risedronate, ibandronate, etidronate, and clodronate) are very hydrophilic and bind avidly to bone mineral (9). Therefore, there is interest in developing less hydrophilic species (10) that might have better activity against tumors in soft tissues and better antibacterial (11) and antiparasitic activity.

The structure of FPPS (from chickens) was first reported by Tarshis et al. (12) and revealed a highly α-helical fold. The structures of bacterial and *Homo sapiens* FPPS (HsFPPS) are very similar; HsFPPS structure (13, 14) is shown in Fig. 2*A*. There are two substrate-binding sites, called here "S1" and "S2." S1 is the allylic (DMAPP, GPP) binding site to which bisphosphonates such as zoledronate bind via a $[Mg^{2+}]_3$ cluster (15) (Fig. 2*B*). S2 is the homoallylic site to which IPP binds, Fig. 2*B*. Recently, Jahnke et al. (10) and Salcius et al. (16) discovered a third ligand-binding site called the "allosteric site" (hereafter the "A site"). A representative zoledronate+A-site inhibitor structure [Protein Data Bank (PDB) ID code 3N46] (Nov_980; compound **6** in Fig. 1) showing zoledronate in S1 and Nov_980 (compound **6**) in the A site is shown in a stereo close-up view in Fig. 2*B*, superimposed on a zoledronate+IPP structure (PDB ID code 2F8Z) in S2. Whether the allosteric site serves a biological function (e.g., in feedback regulation) has not been reported. Nevertheless, highly potent inhibitors (IC_{50} ∼80 nM) have been developed (10), and the best of these newly developed inhibitors are far more hydrophobic than are typical bisphosphonates

Significance

There is an ever-present need for new drugs because of drug resistance. An enzyme called "farnesyl diphosphate synthase" (FPPS) is one important drug target, and drugs called "bisphosphonates" that inhibit this enzyme are of interest both as cancer therapeutics and as antibacterial and antiparasitic drug leads. However, they bind avidly to bone and so are ineffective against most tumors and most infectious organisms. Here, we report the discovery of compounds that lack a bone-binding feature that target FPPS in a unique way, as observed at the atomic level. They also can bind to other protein targets, providing a potentially important approach, multitarget inhibition, that is expected to increase efficacy and decrease the likelihood that resistance will develop.

Author contributions: Y.-L.L., S.L., W.Z., K.W., and E.O. designed research; Y.-L.L., S.L., W.Z., and K.W. performed research; Y.-L.L., S.L., W.Z., K.W., J.A.M., and E.O. analyzed data; and Y.-L.L., S.L., and E.O. wrote the paper.

Reviewer: W.J., Novartis Institutes for Biomedical Research.

The authors declare no conflict of interest.

Data deposition: The atomic coordinates and structure factors have been deposited in the RCSB Protein Data Bank, www.pdb.org [PDB ID codes for FPPS complexed with: taxodione/zoledronate (4P0V), arenarone/zoledronate (4P0W), and taxodione (4P0X)].

[1]Y.-L.L. and S.L. contributed equally to this work.

[2]To whom correspondence may be addressed. E-mail: jmccammon@ucsd.edu or eoldfiel@illinois.edu.

This article contains supporting information online at www.pnas.org/lookup/suppl/doi:10.1073/pnas.1409061111/-/DCSupplemental.

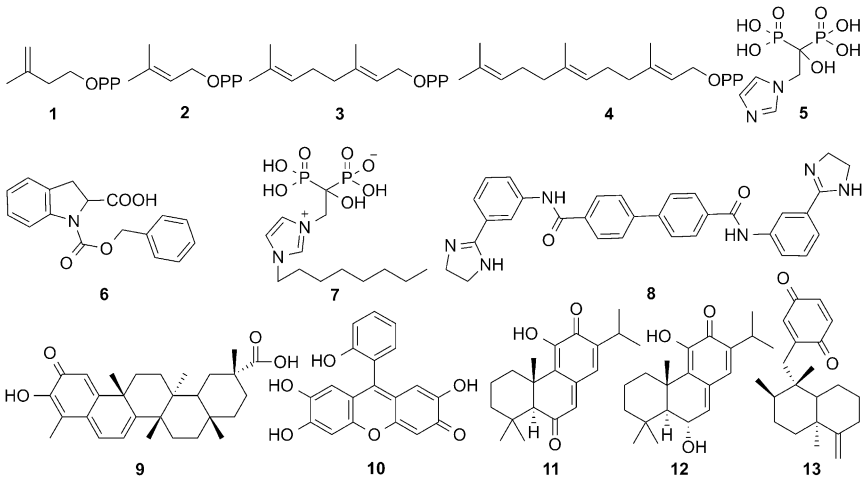

Fig. 1. Chemical structures of FPPS substrates, products, and inhibitors.

(~2.4–3.3 for cLogP vs. ~−3.3 for zoledronate) and are expected to have better direct antitumor effects in soft tissues (10).

In our group we also have developed more lipophilic compounds (e.g., compound **7** in Fig. 1) (17, 18) as antiparasitic (19) and anticancer drug leads (18) and, using computational methods, have discovered other novel nonbisphosphonate FPPS inhibitors (e.g., compound **8** in Fig. 1) that have micromolar activity against FPPS (20). In this study, we extended our computational work and tried to discover other FPPS inhibitors that target the A site. Such compounds would be of interest because they might potentiate the effects of zoledronate and other bisphosphonates, as reported for other FPPS inhibitors (21), and have better tissue distribution properties in general.

Results

Discovery of FPPS Inhibitors. We sought to find FPPS inhibitors by using virtual screening with both X-ray structures and structures obtained from molecular dynamics (MD) simulations. We first carried out an MD simulation of HsFPPS based on the crystal structure of the allosteric site inhibitor Nov_823 (PDB ID code 3N6K), with and without the inhibitor. Full details are given in *Methods and Materials*. The structural ensemble chosen for the virtual screening was representative of both snapshots from the MD simulation and the allosteric site FPPS crystal structures that previously were demonstrated to be valuable in virtual screening (20): PDB ID codes 3N1V, 3N1W, 3N3L, 3N5H, 3N5J, 3N6K, 3N45, 3N46, and 3N49. Structures representing the conformational variability of the allosteric site during the simulations were extracted using clustering in which frames taken every 10 ps were extracted from the MD trajectories. These frames were aligned using all C_α atoms that were within 10 Å of the ligand in the ligand-bound starting structure. Subsequent clustering was performed by rmsd using conformational clustering (22) resulting in five apo and four ligand-bound clusters that represented at least 90% of the trajectories. The total structural ensemble for the virtual screens thus consisted of 18 FPPS structures: nine from the MD simulations, and nine X-ray structures.

Virtual screening was performed using the National Cancer Institute (NCI) diversity set III, a subset of the full NCI compound database. Ligands were prepared using LigPrep (23), adding missing hydrogen atoms and generating all possible ionization states as well as tautomers. The final set used for virtual screening contained 1,013 compounds. Docking simulations were performed with both AutoDock Vina (24) and Glide (25–27). The individual AutoDock Vina and Glide rankings were combined to form a consensus list of compounds that scored well with both methods. The seven top-scoring compounds from AutoDock Vina and Glide, respectively, and the top 36 compounds from the consensus list were chosen as the final 50 compounds for experimental investigation (*SI Appendix*, Fig. S1).

We obtained these 50 compounds from the Drug Synthesis and Chemistry Branch, Developmental Therapeutics Program, Division of Cancer Treatment and Diagnosis, National Cancer Institute (NCI/DTP) and tested them for inhibition of HsFPPS and TbFPPS, the latter being of interest because it is an antiparasitic drug target (28). In an initial screen we tested compounds for FPPS inhibition (29) at an inhibitor concentration of 25 μM. Compounds that showed any inhibition then were retested,

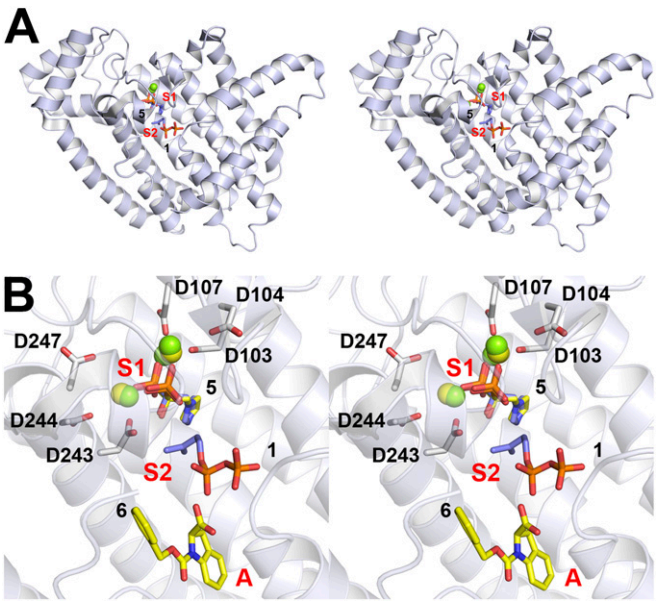

Fig. 2. Structures of human FPPS. (*A*) Structure of HsFPPS showing zoledronate (compound **5**) and IPP (compound **1**) bound to the S1 (allylic) and S2 (homoallylic) ligand-binding sites (PDB ID code 2F8Z). (*B*) Superposition of the IPP-zoledronate structure (PDB ID code 2F8Z) on the zoledronate-Nov_980 A-site inhibitor structure (PDB ID code 3N46). Zoledronate binds to the allylic site S1, IPP binds to the homoallylic site S2, and the allosteric site inhibitor binds to the A site. Active-site "DDXXD" residues are indicated, as are Mg^{2+} molecules (green and yellow spheres, respectively). The views are in stereo.

and a full dose–response curve was obtained. There were two hits: celastrol (compound **9** in Fig. 1) and NSC9037, 2,6,7-trihydroxy-9-(2-hydroxyphenyl)xanthen-3-one (compound **10** in Fig. 1). These compounds had the following IC_{50} values in FPPS inhibition: compound **9:**, TbFPPS, 17 μM and HsFPPS, no activity; compound **10**: TbFPPS, 54 μM; HsFPPS, 81 μM (*SI Appendix*, Table S1). Both compounds are quinone methides, and compound **9** has diverse biological activities (30–33). Therefore we elected to use compound **9** as the basis for a similarity search using the NCI/DTP option in PubChem (https://pubchem.ncbi.nlm.nih.gov/) with compounds again being obtained from the NCI/DTP (http://dtp.cancer.gov). Twenty-five compounds (*SI Appendix*, Fig. S2) were tested against both HsFPPS and TbFPPS. The only compound with activity was NSC122419, the quinone methide taxodione (compound **11** in Fig. 1), which had an IC_{50} of 1.2 μM against HsFPPS (*SI Appendix*, Table S1); in comparison, zoledronate had an IC_{50} of 0.5 μM under the same assay conditions.

We then carried out a second similarity search based on taxodione (compound **11**) and tested 15 compounds (*SI Appendix*, Fig. S3) from the NCI/DTP against HsFPPS. There were two hits with IC_{50} in the 1–3 μM range: the quinone methide taxodone (compound **12** in Fig. 1) and the quinone arenarone (compound **13** in Fig. 1), both of which have been reported to have anti-infective or anticancer activity (34–39). All three terpenoid inhibitors (compounds **11**, **12**, and **13**) thus contain either the hydroxyquinone methide fragment found in the terpenoid celastrol (compound **9**) and compound **10** or a quinone moiety (compound **13**); all three compounds (**11**, **12**, and **13**) are quite active against FPPS (*SI Appendix*, Table S1) and have been reported to be active against tumor cells (35, 40, 41). We also tested compounds **9**, **11,** and **13** against the MCF-7 tumor cell line and found IC_{50} values for cell growth inhibition (*SI Appendix*, Table S1) of 0.2, 2, and 17 μM, respectively. Compounds **11**, **12**, **13** are all slightly more hydrophobic than the A-site inhibitors (10) with cLogP ~4 for taxodione and taxodone, and cLogP ~5 for arenarone, vs. ~3.3 for the most potent A-site inhibitor (10). To see if there was any activity against geranylgeranyl diphosphate synthase (GGPPS), another potential drug target, we tested all hits against an expressed human GGPPS (HsGGPPS). There was much less activity than with FPPS (compound **9**, 32 μM; compound **10**, > 200 μM; compound **11**, 20 μM; compound **12**, 46 μM; compound **13**, 21 μM; *SI Appendix*, Table S1).

X-Ray Crystallographic Investigations. We next sought to investigate how compounds **11**, **12,** and **13** bind to HsFPPS. We were unsuccessful in obtaining crystals containing compound **12** (taxodone), but we did obtain three other crystal structures: taxodione+zoledronate (PDB ID code 4P0V); arenarone+zoledronate (PDB ID code 4P0W), and taxodione alone (PDB ID code 4P0X) in which there were two bound taxodione molecules. Crystals diffracted to 2.4 Å (compound **11**+zoledronate), 2.4 Å (compound **13**+zoledronate), and 2.5 Å (compound **11** alone). Full data acquisition and refinement details are given in Table 1, and experimental details are given in *Materials and Methods*. Ligand electron densities are shown in *SI Appendix*, Fig. S4, and ligand–protein interactions are shown in *SI Appendix*, Figs. S5–S7.

Table 1. Data collection and refinement statistics

Crystal (PDB ID code)	HsFPPS-**5/11** (4P0V)	HsFPPS-**5/13** (4P0W)	HsFPPS-**11/11**(4P0X)
Data collection			
Radiation source	LS-CAT 21-ID-F	LS-CAT 21-ID-F	LS-CAT 21-ID-F
Wavelength, Å	0.97857	0.97857	0.97857
Space group	$P4_12_12$	$P4_12_12$	$P4_12_12$
a, Å	112.14	111.24	110.62
b, Å	112.14	111.24	110.62
c, Å	67.05	67.29	78.44
Resolution, Å*	50.0–2.40 (2.44–2.40)	50.0–2.40 (2.44–2.40)	50.0–2.30 (2.34–2.30)
No. of reflections	17,015 (828)	16,815 (820)	22,231 (1,103)
Completeness, %	98.5 (100.0)	99.7 (100.0)	99.8 (100.0)
Redundancy	8.1 (7.7)	26.0 (26.5)	11.0 (11.1)
R_{merge}, %	8.1 (57.8)	10.9 (32.6)	7.7 (64.5)
I/s(I)	35.8 (4.4)	76.5 (16.5)	44.0 (4.6)
Refinement			
Resolution, Å*	50.0–2.40 (2.46–2.40)	50.0–2.40 (2.46–2.40)	50.0–2.50 (2.57–2.50)
No. of reflections	16,076 (1175)	15,618 (835)	16,446 (880)
R_{work}, %	20.6 (23.6)	20.4 (26.0)	20.7 (26.4)
R_{free}, %	29.2 (33.0)	28.9 (33.9)	27.9 (32.9)
Geometry deviations			
Bond lengths, Å	0.014	0.017	0.016
Bond angles, °	1.575	1.791	1.760
Mean B-values. $Å^2$/no. non-H atoms			
All refined atoms	57.5/2,880	50.9/2,904	50.5/2,764
Compound atoms	55.2/39	40.8/39	60.4/46
Mg ions	42.7/3	27.1/3	
Water molecules	49.8/32	41.1/56	42.7/61
Ramachandran plot, %			
Most favored	91.7	93.3	92.8
Additionally allowed	8.3	6.7	7.2
Generously allowed	0	0	0
Disallowed	0	0	0

*Values in parentheses are for the highest-resolution shells.

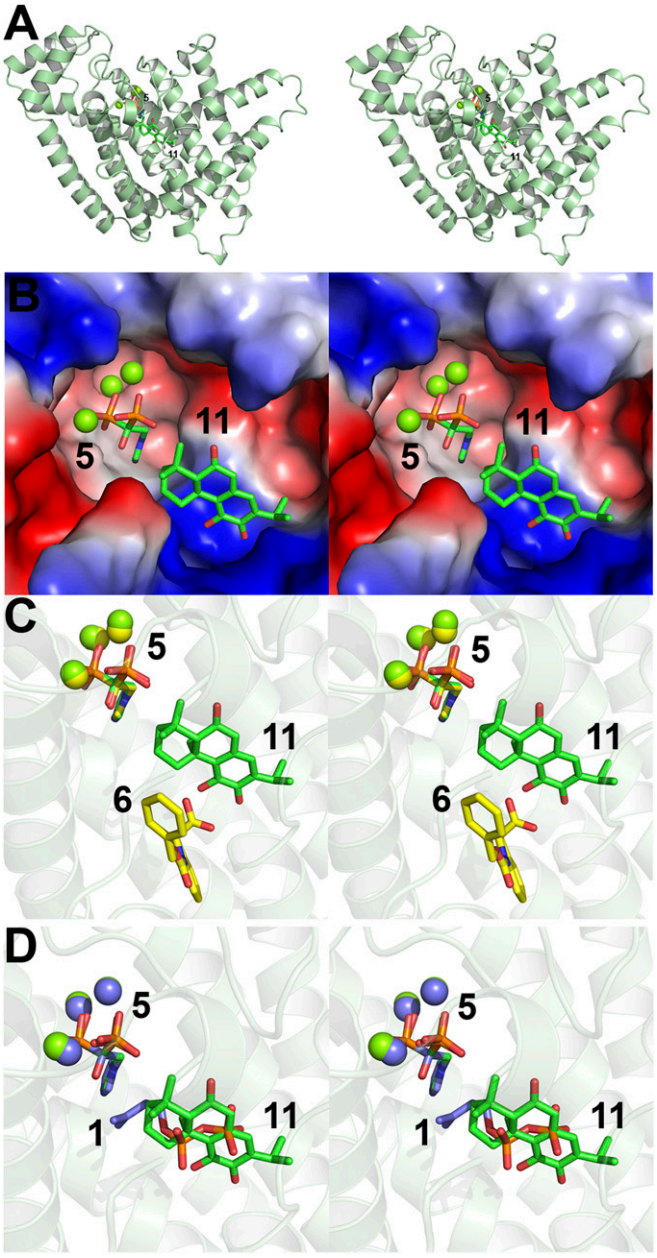

Fig. 3. Structures of taxodione (compound **11**)+zoledronate+Mg^{2+} (compound **5**) bound to HsFPPS (PDB ID code 4P0V). (*A*) Stereo view of the taxodione+zoledronate+Mg^{2+} structure. (*B*) Close-up view of bound ligands. (*C*) Superposition of the taxodione+zoledronate+Mg^{2+} structure with the zoledronate+Nov_980+Mg^{2+} structure (PDB ID code 3N46). (*D*) Superposition of the taxodione+zoledronate structure with zoledronate+IPP structure (PDB ID code 2F8Z). Taxodione binds to the IPP site, S2. The views are in stereo.

Taxodione (compound **11**) crystallized together with one molecule of zoledronate (compound **5**) and three Mg^{2+}; stereo views of the structure (PBD ID code 4P0V) are shown in Fig. 3 *A* and *B*. Zoledronate binds, as expected, to the S1 site via three Mg^{2+} and there is a 0.3-Å rmsd between all zoledronate atoms and Mg^{2+} in the taxodione+zoledronate+Mg^{2+} structure vs. the zoledronate+IPP+Mg^{2+} alone structure (PDB ID code 2F8Z). However, the taxodione ligand does not bind to the A site found with the Novartis inhibitor compound **6** (PDB ID code 3N46) (shown superimposed on the taxodione+zoledronate+Mg^{2+} structure in Fig. 3*C*). It is particularly interesting that the quinone methide fragment in this taxodione+zoledronate structure occupies the IPP diphosphate-binding site (Fig. 3*D*). No other FPPS inhibitors (except for *S-thiolo*-IPP) bind to this S2 site.

As noted above, there are two ligand-binding sites in FPPS. The S1 site contains primarily the two DDXXD motifs involved in binding to the three Mg^{2+} and the allylic substrate, DMAPP, with Mg^{2+} facilitating diphosphate ionization. In Table 2 we show the results of a SCORECONS analysis (42), which ranks residues in terms of their essential nature: A score of 1.000 means the residue is essential; a residue with a score of 0 is nonessential. The top 20 residues (minus structural G and P residues) are shown in Table 2 together with their ligand interactions. As can be seen in Table 2, in addition to the catalytic Asps, numerous highly conserved Arg/Lys residues, including K57, R60, R112 and R113, K57, R60, and R113, are involved in electrostatic/hydrogen bond interactions with the IPP ligand in S2 (Fig. 4*A*). Notably, R60 and R113 also are the ligands that are very close to the taxodione carbonyl and OH groups (Fig. 4*B*); a LigPlot (43) view of these interactions is shown in *SI Appendix*, Fig. S5.

We next obtained the structure of taxodione (compound **11**) alone bound to HsFPPS (PDB ID code 4P0X). Full data acquisition and structure refinement details are given in Table 1, and experimental details are given in *Materials and Methods*. Electron densities are given in *SI Appendix*, Fig. S4*B*. Crystallization was carried out in the presence of Mg^{2+} and GPP, but only taxodione was present in the crystals. Full and expanded stereoview structures are shown in Fig. 5 *A* and *B*, and Fig. 5*C* shows the superposition of the taxodione (cyan ligands)+zoledronate structure (PDB ID code 4P0V) and the taxodione-only (magenta and orange ligands) structure (PDB ID code 4P0X). All protein–ligand interactions are shown in *SI Appendix*, Fig. S6. *SI Appendix*, Figs. S5 and S6 show that one taxodione molecule (orange in Fig. 5*B* and *SI Appendix*, Fig. S6*B*) is located near the protein surface, and the second taxodione molecule (magenta), is bound to the IPP site and interacts with N59 and with the water molecules, R60, E93, Q96, and Q240.

Finally, we determined the structure of the arenarone+zoledronate+Mg^{2+} complex (PDB ID code 4P0W). Full data acquisition and structure refinement details are given in Table 1, and ex-

Table 2. Top SCORECONS scores of HsFPPS

Rank	Residue no.	Amino acid	SCORECONS	Interacting ligands
1	240	Q	0.912	**1, 2**
2	244	D	0.900	Mg^{2+}
3	112	R	0.871	**2, 5, 11, 13**
4	243	D	0.840	Mg^{2+}, **1, 5, 11**
5	113	R	0.835	**1, 11, 13**
6	104	D	0.833	Mg^{2+}
7	103	D	0.831	Mg^{2+}, **5**
8	100	L	0.828	**5, 11, 13**
9	261	D	0.826	Mg^{2+}
10	200	K	0.823	**2, 5**
11	60	R	0.819	**1, 11, 13**
12	57	K	0.811	**1, 11, 13**
13	239	F	0.809	**1, 11, 13**
14	96	Q	0.807	**1, 11, 13**
15	201	T	0.804	**1, 2, 5**
16	353	K	0.797	**1, 11**
17	93	E	0.795	**1, 11, 13**
18	107	D	0.788	Mg^{2+}, **5**
19	351	R	0.783	**1**
20	257	K	0.780	**1, 5, 11**

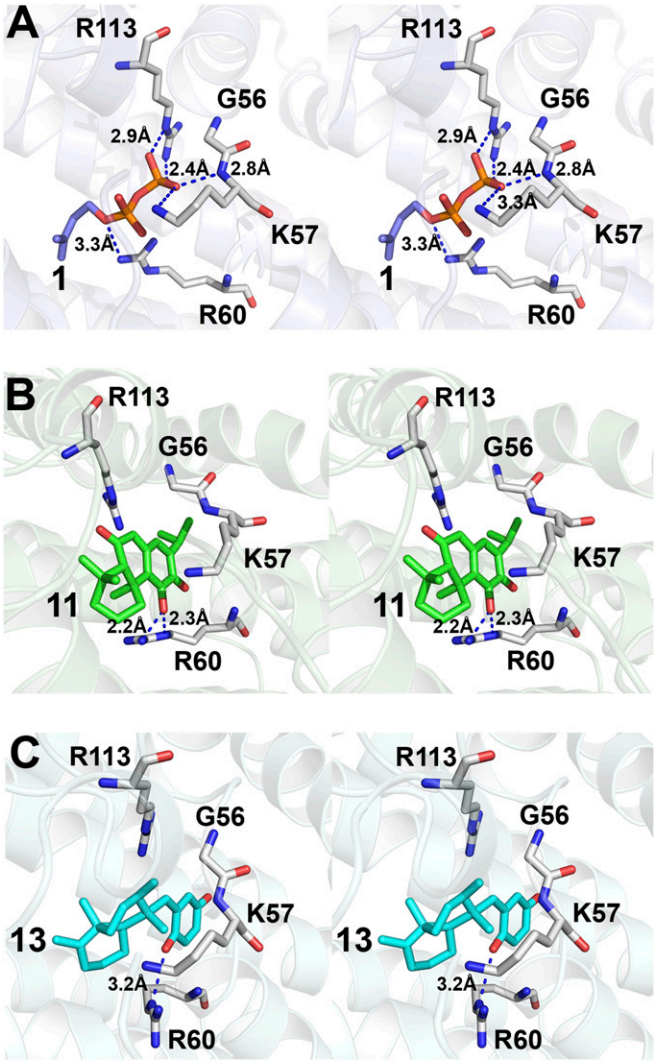

Fig. 4. Protein–ligand interactions in the IPP-binding site. (*A*) IPP (PDB ID code 2F8Z). (*B*) Taxodione from the taxodione+zoledronate structure (PDB ID code 4P0V). (*C*) Arenarone (PDB ID code 4P0W). The views are in stereo.

perimental details are given in *Materials and Methods*. Electron densities are shown in *SI Appendix*, Fig. S4*C*. Ligand–protein interactions are shown in *SI Appendix*, Fig. S7. The structure (Fig. 6 *A* and *B*) is quite similar to that seen in the taxodione+zoledronate+Mg^{2+} complex, with arenarone again occupying the IPP site, S2 (Fig. 6*C*), and Arg60 again being in close proximity to one ligand, carbonyl oxygen (Fig. 4*C* and *SI Appendix*, Fig. S7). Superposition of the taxodione+zoledronate+Mg^{2+}, arenarone+zoledronate+Mg^{2+}, and **6**+zoledronate+Mg^{2+} structures in Fig. 6*D* again shows that taxodione and arenarone do not bind to the allosteric site A; presumably, the initial hit (celastrol) was detected because the pocket used in the in silico screen extends into the IPP pocket.

A Principal Component Analysis of FPPS Structures. The results described above are of interest because they show an unusual FPPS inhibitor binding mode, so we next investigated how these protein structures compared with previously reported HsFPPS structures. We first used the POVME program (44) to measure pocket volumes (for apo and deliganded structures). The results in *SI Appendix*, Table S2 clearly show that the open and closed pockets are quite distinct. The pockets found in apo, taxodione-only, and the Novartis allosteric site-only inhibitors are open and have volumes of 858 ± 24 $Å^3$, whereas the closed pockets have volumes of 508 ± 50 $Å^3$ (*SI Appendix*, Table S2). In each case the closed pocket structures contain one bisphosphonate.

We then used principal component analysis (PCA) to analyze all these HsFPPS structures. PCA mathematically converts a number of possibly correlated multivariables into sets of linearly uncorrelated variables through orthogonal transformation, thereby reducing the dimensionality, or the number of variables, of the dataset. The first PC describes the largest variance in the dataset, allowing the data to spread most along PC 1. Each successive PC describes the next largest variance orthogonal to the previous PCs. We used PCA because in other work [on undecaprenyl diphosphate synthase (UPPS)] we found we could separate UPPS structures into open, closed, and semiopen states based on a 2D method, that is, using two principal components (PCs), whereas a 1D volume-only–based method did not permit such clustering. We sought to go beyond the volume-only descriptions of the structures.

The 39 structures (the three reported here plus 36 others) formed only two clusters: the open conformations noted above that were centered around PC1 = −30 Å, PC2 = 0 Å and the closed conformations noted above that were centered around PC1 = 10 Å, PC2 = 0 Å (Fig. 7*A*). All the structures in the open

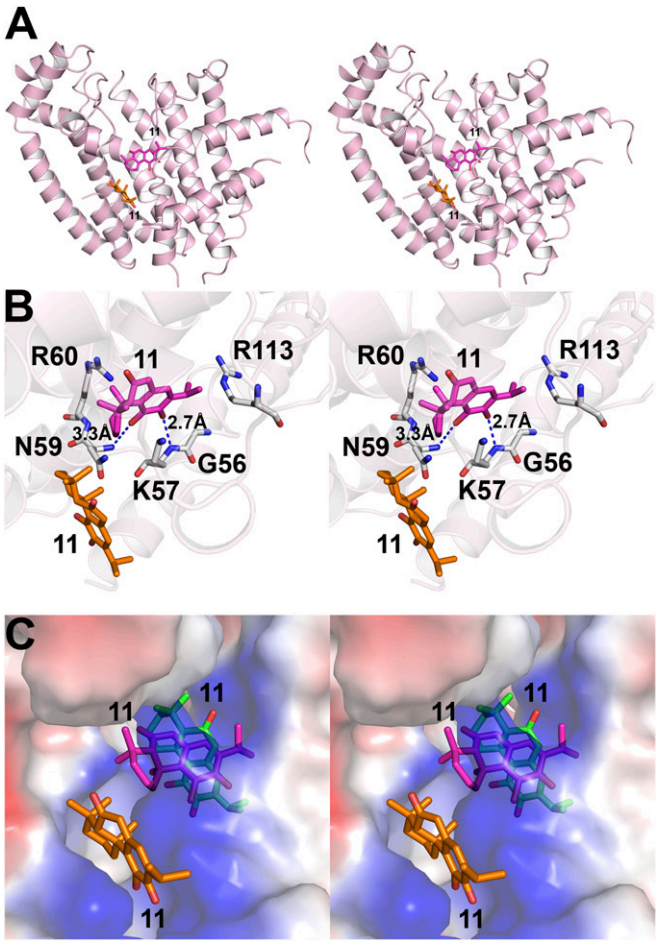

Fig. 5. Structure of taxodione bound to HsFPPS in the absence and presence of zoledronate. (*A*) Full structure (PDB ID code 4P0X) showing two taxodione ligands. (*B*) Expanded view of *A* showing the buried (magenta) and more solvent exposed (orange) taxodione ligands. (*C*) Superposition of the taxodione (PDB ID code 4P0X) (*Left*) and taxodione+zoledronate structures (PDB ID code 4P0V) (*Right*) showing similar locations of the buried taxodiones. The views are in stereo.

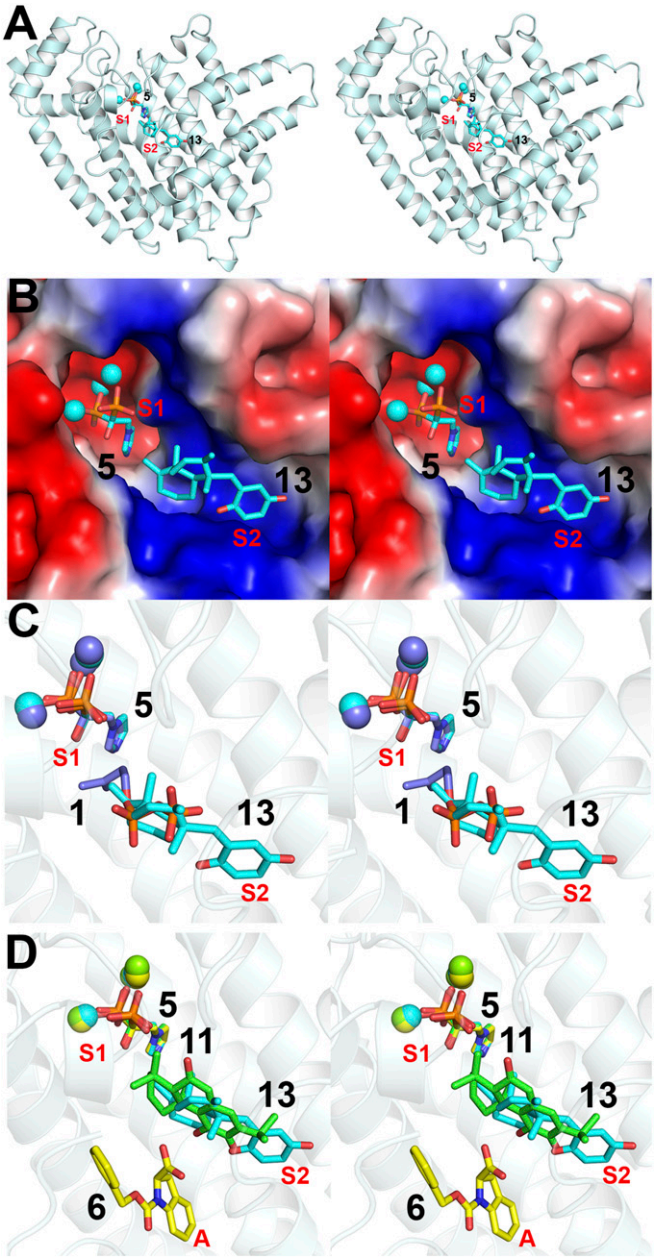

Fig. 6. Structure of arenarone+zoledronate bound to HsFPPS (PDB ID code 4P0W) and a comparison with the structures of taxodione+zoledronate (PDB ID code 4P0V) and Nov_980+zoledronate (PDB ID code 3N46). (*A*) Arenarone+zoledronate (PDB ID code 4P0W). (*B*) Expanded version of *A*. (*C*) Superposition of the arenarone+zoledronate (PDB ID code 4P0W) and IPP+zoledronate (PDB ID code 2F8Z) structures showing S2 binding of arenarone. (*D*) Superposition of the taxodione+zoledronate (PDB ID code 4P0V), arenarone+zoledronate (PDB ID code 4P0X), and Nov_980+zoledronate (PDB ID code 3N46) structures. The three zoledronate-binding poses are all very similar, whereas both taxodione and arenarone bind to S2, the IPP site, not to the A site. The views are in stereo.

form shown in Fig. 7*A* (2F7M, 2N1V, 3N1W, 3N3L, 3N49, 3N5H, 3N5J, 3N6K, 1FPS, and 4P0X) are either apo, allosteric site inhibitor (alone), or taxodione-alone liganded structures, whereas all the closed structures (4GA3, 3RYE, 3S4J, 4DEM, 4H5D, 4H5E, 4H5C, 4JVJ, 4L2X, 2RAH, 2VF6, 1YQ7, 1YV5, 2OPN, 2OPM, 3B7L, 2F89, 2F8C, 2F8Z, 2F92, 2F94, 2F9K, 3N45, 3N46, 1ZW5, 2QIS, 4P0V, and 4P0W) contain a bisphosphonate and Mg^{2+} (in some cases in addition to another ligand, such as taxodione, IPP, or one of the allosteric site inhibitors plus zoledronate). The two types of cluster or structure apparently originate from bisphosphonate binding via Mg^{2+} to the DDXXD motifs (Fig. 2*B*) and, as proposed previously (10), arise from the movement of the C terminus starting around residue 230, which here correlates with a major change in PC1 (Fig. 7*B*).

These results raise the question as to which states are sampled in the two MD simulations used in the virtual screening. Results for the apo-FPPS simulation projected onto PC space are shown in Fig. 7*C*, and results for the liganded form (Nov_823/PDB ID code 3N6K) are shown in Fig. 7*D*. Both simulations start in the open state. However, as shown in Fig. 7*C*, the apo form simulation samples, primarily, partially closed conformations with a PC1 ∼−8Å, whereas the ligand-bound simulation exhibits two distinct conformational distributions: an open conformation (PC1 ∼−25Å) and a partially closed conformation (PC1 ∼−3Å), indicating that the ligand prevents pocket closing and thus perhaps providing a basis for the designation "allosteric."

Differential Scanning Calorimetry. These PCA and pocket volume observations raise the interesting question: Do taxodione and arenarone alone increase the folded to unfolded transition temperatures (T_m), in differential scanning calorimetry experiments? As shown by Rondeau et al. (13), the addition of bisphosphonates to FPPS in the presence of Mg^{2+} increases T_m by up to 25 °C (in the case of zoledronate). Bisphosphonates with weaker inhibitory potency result in smaller T_m shifts, but the addition of IPP to each bisphosphonate raises T_m, with the effects being largest with the weakest inhibitors. Inhibitors generally increase T_m values in proteins, but decreases in T_m also are possible on ligand binding, e.g., as found with ATP binding to the glucose transporter GLUT-1 (ΔT_m ∼−12 °C) (45), or cyclodextrins binding to lysozyme (ΔT_m ∼−10 °C) (46).

In Fig. 8 we show differential scanning calorimetry (DSC) results for HsFPPS (+Mg^{2+}) alone or in the presence of zoledronate at a ligand:protein molar ratio of 10:1 (ΔT_m ∼25 °C), as well as in the presence of 1, 2, and 10 taxodione molecules per protein, arenarone at a ligand:protein molar ratio of 10:1, and taxodione+zoledronate at a ligand:protein molar ratio of 10:1.

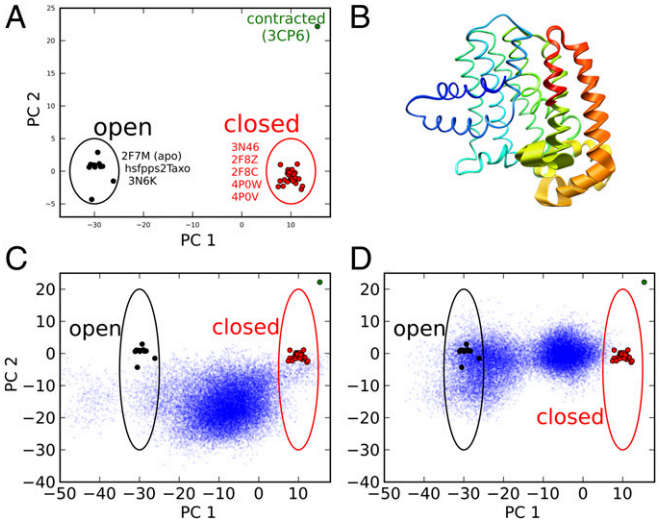

Fig. 7. PCA of HsFPPS structures; units are in Ångstroms. (*A*) Thirty-nine HsFPPS structures showing clustering into open and closed groups (in PC space). (*B*) Structural representation of variation along PC1. (*C*) PCA obtained by using an apo-FPPS trajectory (PDB ID code 3N6K, minus the ligand) showing the dominance of partially closed structures. (*D*) PCA using the liganded structure (PDB ID code 3N6K) for MD showing many more open structures.

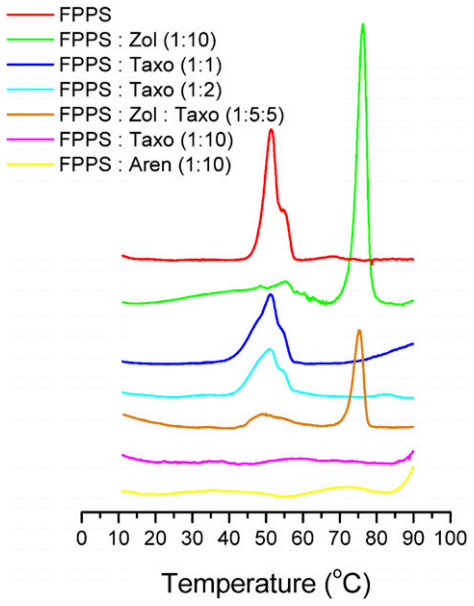

Fig. 8. Differential scanning calorimetry of HsFPPS + 5 mM Mg^{2+} in the presence or absence of zoledronate (Zol) (compound **5**), taxodione (Taxo) (compound **11**) or arenarone (Aren) (compound **13**) at the ligand:protein molar ratios indicated. Zoledronate causes a large (~25 °C) increase in T_m, the maximum in the thermogram of the native-to-unfolded transition. The terpenoid inhibitors broaden the transition.

As can be seen in Fig. 8, there is no increase in T_m with either taxodione or arenarone. Rather, with taxodione the endotherm broadens at molar ratios of 1:1 and 2:1 and is not detectable at a taxodione:FPPS molar ratio of 10:1. Likewise, no endotherm is detected in the presence of arenarone at a ligand:FPPS molar ratio of 10:1. These results are consistent with the observation that, unlike the situation with bisphosphonate/Mg^{2+} binding, the FPPS/taxodione structure more closely resembles the apo structure in terms of PC1 clustering and pocket volume and thus has an unfolding transition that is similar in terms of T_m to that seen with the ligand-free protein. However, the observation that the transition is not visible at higher ligand concentrations was unexpected and perhaps suggests that multiple taxodione molecules may bind to the unfolded protein; this observation, although perhaps somewhat speculative, would be consistent with the presence of two ligand-bound populations in the zoledronate+taxodione system (Fig. 8*D*).

Structure of the Taxodione/*N*-Acetyl Cysteine Adduct. The first hit we obtained from the in silico screen was the quinone methide celastrol (compound **9**). This compound, extracted from Thunder of God vines, is a component of traditional Chinese medicines and has been of interest in the context of the development of therapeutics to treat a wide range of diseases (30–32, 47). Early work suggested inhibition of Hsp90•Cdc37 (48), but more recently several other targets, including annexin II and β-tubulin, have been reported (49). This quinone methide is reported to react with proteins via Michael addition (49, 50) of cysteine thiol groups to form the adduct compound **14** (Fig. 9). Like celastrol (compound **9**), taxodione is a quinone methide that reacts with protein cysteine thiol groups, as was noted as early as 1970 with phosphofructokinase (51). In addition, as does celastrol, taxodione is reported to have diverse biological activities (35, 38, 52). This chemical reactivity, if combined with FPPS inhibition, might lead to potent multitarget inhibitors, perhaps including more tumor-specific (e.g., ras-bearing) targets.

To investigate how thiols might bond to taxodione, we used NMR and mass spectrometry. The high-resolution mass spectrum of a 1:1 taxodione:*N*-acetyl cysteine mixture indicated the formation of a 1:1 adduct, *SI Appendix*, Fig. S8*A*. However, as shown in Fig. 9*A*, there are four possible taxodione sites at which cysteine thiols might bind, leading to compounds **15**–**18**, and certainly there are many possible stereoisomers. Nucleophilic attack at C2, C4, or C6 in celastrol has been proposed to be possible (50); with taxodione, an additional binding site would be to the second carbonyl group (to form compound **18**). A ^1H NMR spectrum of the product is shown in *SI Appendix*, Fig. S8*B* and indicates only a single aromatic proton (Fig. 9*B* shows the downfield region), consistent with formation of the Michael adduct compound **17**. The gradient-selected COSY spectrum (*SI Appendix*, Fig. S8*D*) confirms this structure. The NOESY spectrum (*SI Appendix*, Fig. S8*C*) exhibits the NOE correlations shown in Fig. 9*C* and indicates regiospecific, stereoselective addition leading to the product shown in Fig. 9*D* [basically the behavior reported in ref. 50 with celastrol, which binds several nucleophiles at the same site (48, 50)].

However, the inhibition effects we see with HsFPPS are not the result of covalent enzyme modification. If we use 100-μM enzyme concentrations (100× that in the inhibition assays) as well as 100-μM inhibitor concentrations, we can see (via electrospray-ionization mass spectrometry; *SI Appendix*, Fig. S9 *A* and *B*) that approximately one in three FPPS has one bound taxodione, but this reaction would be ~10,000 times slower in the enzyme inhibition assays in which the both enzyme and inhibitor concentrations are ~1 μM. The same effect is seen with celastrol/FPPS: About one in two FPPS is modified (*SI Appendix*, Fig. S9*C*), but here celastrol is not even an inhibitor of HsFPPS.

Conclusions

The results presented above are of interest for several reasons. First, we used in silico screening to discover inhibitors of farnesyl diphosphate synthase. Using MD-based methods followed by in silico and in vitro screening, we found that the triterpenoid celastrol, a quinone methide, inhibited *Trypanosoma brucei* FPPS (TbFPPS) with an IC_{50} ~20 μM. We then carried out two rounds of similarity searching leading to three leads having IC_{50} values in the 1–3 μM range against human FPPS (as compared with 0.5 μM for zoledronate, under the same assay conditions). All three compounds were terpenoids: taxodone, taxodione, and arenarone. We then determined the structures of taxodione and arenarone bound to human FPPS. The unexpected result was that both terpenoids bound to the homoallylic, IPP-binding site (S2) and not to the allosteric site A, as might have been expected. The basis for this binding to the IPP site is that there are interactions between the ligand oxygen molecules and the highly conserved Arg and Lys residues that normally bind to the IPP substrate's diphosphate group with the hydrophobic terpenoid fragment interacting with a more hydrophobic site. The observation that celastrol and taxodione are both quinone methides that bind to several proteins via Michael addition (to protein thiols) and have been of interest as anticancer and antiinfective drug leads suggests that in the future it may be possible to develop analogs that more potently inhibit FPPS to provide novel multitarget inhibitors, based in part on the structural results presented here.

Methods and Materials

Computational Aspects. ***MD simulations of FPPS and cluster analysis.*** Systems prepared for simulations were based on the crystal structure (PDB ID code 3N6K) with the highest-affinity FPPS allosteric site inhibitor, 1-(carboxymethyl)-1H-benzo[g]indole-2-carboxylic acid (10). Two different systems were built: apo and ligand-bound. Tleap (53) was used to neutralize the systems by adding Na^+ counter ions and solvating using a TIP3P water box. The fully solvated apo system contained 63,913 atoms, whereas the fully solvated ligand-bound system contained 65,359 atoms. Simulations were performed on each system

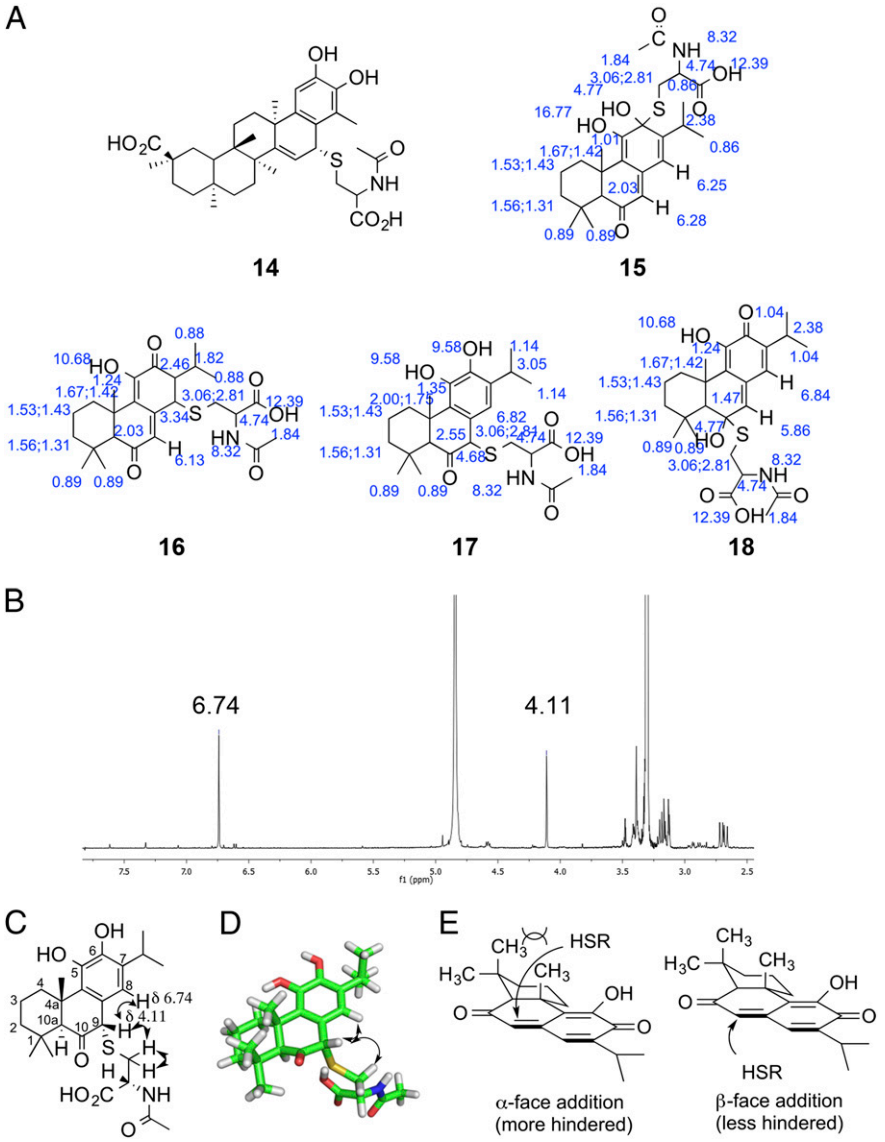

Fig. 9. Structures of quinone-methide adducts. (*A*) Structure of a celastrol (compound **9**)-thiol adduct (compound **14**), based on refs. 48 and 50 together with four potential taxodione/*N*-acetyl cysteine adducts (compounds **15**–**18**) together with their ^{1}H NMR chemical shifts predicted using ChemDraw (71) (in blue). Many other stereoisomers are possible; those shown are illustrative of the four sites of attachment (needed for NMR shift predictions). (*B*) Downfield region of the 400-MHz ^{1}H NMR spectrum of the taxodione/*N*-acetyl cysteine adduct showing only a single (aromatic) proton resonance in the downfield aromatic/olefinic chemical shift region (6.74 ppm observed, 6.82 ppm calculated, from internal tetramethylsilane) consistent with regiospecific Michael addition (as observed also with celastrol). Only two stereoisomers are possible here. (*C*) Summary of key nuclear Overhauser effect connectivities (from the spectrum in *SI Appendix*, Fig. S8). (*D*) Proposed structure of the taxodione/*N*-acetyl cysteine adduct showing stereospecific addition to the less sterically hindered face of the molecule. (*E*) Two possible routes for nucleophile addition. Only one isomer is formed as seen by NMR.

independently. Minimization using SANDER (53) was carried out in two stages: 1,000 steps of minimization of solvent and ions with the protein and ligand restrained using a force constant of 500 kcal^{-1}·mol^{-1}·Å^2, followed by a 2,500-step minimization of the entire system. An initial 20-ps MD simulation with weak restraints (10 kcal^{-1}·mol^{-1}·Å^2) on the protein and ligand atoms then was used to heat the system to 300 K. Subsequently, 100-ns MD simulations were performed on both systems under constant temperature/constant pressure ensemble conditions at 300 K using AMBER (53) and the ff99SBildn force field (54, 55). Periodic boundary conditions were used, along with a nonbonded interaction cutoff of 10 Å. Bonds involving hydrogen atoms were constrained using the SHAKE algorithm (56) with 2-fs time steps.

Pocket-Volume Calculations. To quantify the degree of openness of the structures seen in the PCA, we calculated the volume of the central protein pocket (containing the Mg^{2+}, IPP, and zoledronate-binding sites). POVME (44) was used for pocket-volume calculations. The crystal structure of HsFPPS in complex with zoledronate and isopentenyl diphosphate (PDB ID code 2F8Z) was used as the reference structure. The coordinates of the following atoms were used as centers for POVME inclusion spheres: all three Mg^{2+}, PA, PB, O3A, C1, and C3 of IPP, and P9, P14, C8, C18, and N15 of zoledronate. All proteins were superimposed onto 2F8Z, and all nonprotein atoms were removed for the volume calculations. Points were generated in POVME with a grid spacing of 1 Å using inclusion spheres with a 5-Å radius around the atom positions. The volume was calculated using the contiguous option (with contiguous seed spheres with a 3-Å radius centered at the same coordinates as the inclusion spheres).

PCA. The PCA was performed using the Bio3D package in R (57). The PC space was built up using 36 reported HsFPPS structures together with the three structures described here. The resulting 39 structures underwent iterative rounds of structural superposition to determine the invariant core of the protein, a region that exhibits the least structural variance among all the protein structures. This core consists of residues 21, 23–25, 45–54, 58–72, 77–106, 109–112, 115–120, 124–175, 177, 193–196, 198–201, 207–219, 225–226, 228, and 231–233. Subsequently, the experimental structures were super-

imposed onto this core, and a PCA was used (58, 59). All the experimental structures projected into the space spanned by PC1 and PC2, along which there is the most variance. The first two PCs account for 93% of all of the variance observed, and PC1 alone accounts for 88.7% of the variance observed. The PC space generated from the experimental structures served as the basis for the projection of the MD trajectories.

Experimental Aspects. ***Expression and purification of HsFPPS, TbFPPS, and HsGGPPS.*** The expression and purification of TbFPPS, HsFPPS, and HsGGPPS followed the protocols reported previously (17, 60, 61).

Protein crystallization, data collection, and refinement. Crystallization of HsFPPS followed the protocol reported previously with minor modifications (62). HsFPPS (23 mg/mL) was incubated with 5 mM $MgCl_2$ and 1 mM taxodione and 1 mM zoledronate or 1 mM taxodione and 1 mM GPP or 1 mM arenarone and 1 mM zoledronate. The mixtures were incubated on ice for 3 h, and any precipitates formed were removed by centrifugation (17,000 × *g* for 5 min). HsFPPS plus inhibitor solutions then were mixed in a 1:1 ratio with reservoir buffer [1.2 M phosphate buffer (pH 5.0), 25% glycerol]. Protein and ligands mixtures were incubated using the hanging-drop method at 20 °C until hexagonal crystals appeared. Crystals then were mounted and frozen in liquid nitrogen. Diffraction data were collected at the Life Sciences Collaborative Team (LS-CAT) beam-line 21ID-F at the Argonne National Laboratory. Data were processed by using HKL3000 (63) and refined by using CCP4 (64) and Coot (65). The LigPlots (43) and Ramachandran plots were generated by Ligplot+ (66) and PDBsum (67), respectively. Protein and ligand structures were drawn using PyMOL (68).

Enzyme inhibition. HsFPPS, TbFPPS, and HsGGPPS inhibition assays were carried out as described previously (17, 20, 62). Compounds first were screened at 25 μM using a PPi release assay (69); then full dose–response curves were obtained for the actives, and IC_{50} values were obtained using the Prism program (www.graphpad.com). The screening libraries were obtained from the Drug Synthesis and Chemistry Branch, DPT/NCI. The purity of key compounds is shown in *SI Appendix*, Fig. S10.

Inhibition of tumor-cell growth. MCF-7 cell growth inhibition assays followed the basic protocol described previously (70) with slight modifications. Cells were subcultured in DMEM plus 10% (vol/vol) FBS. Cells were grown at 37 °C in a 5% (vol/vol) CO_2 atmosphere. Five thousand cells per well were inoculated with compounds in a total of 90 μL medium covered with a gas-permeable sealing membrane (catalog no. BEM-1; Diversified Biotech) and wrapped by Parafilm, to avoid evaporation. Plates then were incubated for 4 d at 37 °C in 5% CO_2. Cancer cell inhibition assays were carried out by using a 3-(4,5-dimethylthiazole-2-yl)-2,5-diphenyltetrazolium bromide (MTT) cell proliferation assay kit (30–1010K; ATCC). After incubation, 10 μL of MTT reagent was added to each well, and plates were incubated for 3 h at 37 °C in a 5% CO_2 atmosphere. After incubation, 100 μL of detergent (SDS) was added to each well to stop the reaction. After overnight incubation at room temperature in the dark, cell densities were counted by using a UV-VIS spectrophotometer at 570 nm. Dose–response curves and corresponding IC_{50}s were fitted by using program Prism (www.graphpad.com).

DSC. DSC experiments were carried out using a Microcal VP-DSC instrument. The HsFPPS protein concentration was 30 μM in 25 mM Tris buffer (pH 7.5), 25 mM NaCl, and 5 mM $MgCl_2$. Zoledronate was added from an aqueous stock solution; taxodione and arenarone were from 20-mM stock solutions in DMSO. DMSO [final percentage ∼1.5% (vol/vol)] had no effect on the thermal transition. The scans covered the range of 10 °C to 90 °C at a scan rate of 10 °C/h for all systems. All transitions were irreversible. The DSC thermograms were processed by using Origin 7.1 software (www.sigmaplot.com). Buffer vs. buffer scans were used for baseline correction.

Electrospray-ionization mass spectrometry. Spectra of 100 μM HsFPPS in the absence or presence of 100 μM taxodione (compound **11**) or celastrol (compound **9**) were obtained by using a Waters Quattro Ultima electrospray ionization mass spectrometry system (Waters Corp.). Samples were incubated in 10 mM Tris (pH 7.4), 25 mM NaCl, 100 μM inhibitor, 0.5% DMSO, for 15 min at 23 °C.

ACKNOWLEDGMENTS. We thank Roberto Docampo and Andrea Montalvetti for providing the TbFPPS expression system; Hiroshi Sagami for providing the HsGGPPS system; Howard Robinson for data analysis; the NCI/DPT Open Chemical Repository for providing compounds; Gary Turner and Ted Turner of Spectral Data Services Incorporated for obtaining the NMR spectra; and Yang Wang for helpful suggestions. This work was supported by the US Public Health Service [National Institutes of Health (NIH) Grants GM065307 and CA158191 (to E.O.)]. Use of the Advanced Photon Source, an Office of Science User Facility operated for the US Department of Energy (DOE) Office of Science by Argonne National Laboratory, was supported by the US DOE under Contract no. DE-AC02-06CH11357. Use of the LS-CAT Sector 21 was supported by the Michigan Economic Development Corporation and Grant 085P1000817 from the Michigan Technology Tri-Corridor. Work at the University of California, San Diego was supported in part by the NIH, the National Science Foundation (NSF), the Howard Hughes Medical Institute, the National Biomedical Computation Resource, the Center for Theoretical Biological Physics, and the NSF Supercomputer Centers. S.L. was supported by American Heart Association Grant 12POST11570005.

1. Oldfield E, Lin FY (2012) Terpene biosynthesis: Modularity rules. *Angew Chem Int Ed Engl* 51(5):1124–1137.
2. Liu CI, et al. (2008) A cholesterol biosynthesis inhibitor blocks *Staphylococcus aureus* virulence. *Science* 319(5868):1391–1394.
3. Russell RG (2011) Bisphosphonates: The first 40 years. *Bone* 49(1):2–19.
4. Martin MB, et al. (2001) Bisphosphonates inhibit the growth of *Trypanosoma brucei, Trypanosoma cruzi, Leishmania donovani, Toxoplasma gondii*, and *Plasmodium falciparum*: A potential route to chemotherapy. *J Med Chem* 44(6):909–916.
5. Kunzmann V, Bauer E, Wilhelm M (1999) Gamma/delta T-cell stimulation by pamidronate. *N Engl J Med* 340(9):737–738.
6. Coscia M, et al. (2010) Zoledronic acid repolarizes tumour-associated macrophages and inhibits mammary carcinogenesis by targeting the mevalonate pathway. *J Cell Mol Med* 14(12):2803–2815.
7. Shipman CM, Croucher PI, Russell RG, Helfrich MH, Rogers MJ (1998) The bisphosphonate incadronate (YM175) causes apoptosis of human myeloma cells in vitro by inhibiting the mevalonate pathway. *Cancer Res* 58(23):5294–5297.
8. Wood J, et al. (2002) Novel antiangiogenic effects of the bisphosphonate compound zoledronic acid. *J Pharmacol Exp Ther* 302(3):1055–1061.
9. Mukherjee S, Huang C, Guerra F, Wang K, Oldfield E (2009) Thermodynamics of bisphosphonates binding to human bone: A two-site model. *J Am Chem Soc* 131(24): 8374–8375.
10. Jahnke W, et al. (2010) Allosteric non-bisphosphonate FPPS inhibitors identified by fragment-based discovery. *Nat Chem Biol* 6(9):660–666.
11. Leon A, et al. (2006) Isoprenoid biosynthesis as a drug target: Bisphosphonate inhibition of *Escherichia coli* K12 growth and synergistic effects of fosmidomycin. *J Med Chem* 49(25):7331–7341.
12. Tarshis LC, Yan M, Poulter CD, Sacchettini JC (1994) Crystal structure of recombinant farnesyl diphosphate synthase at 2.6-A resolution. *Biochemistry* 33(36):10871–10877.
13. Rondeau JM, et al. (2006) Structural basis for the exceptional in vivo efficacy of bisphosphonate drugs. *ChemMedChem* 1(2):267–273.
14. Kavanagh KL, et al. (2006) The molecular mechanism of nitrogen-containing bisphosphonates as antiosteoporosis drugs. *Proc Natl Acad Sci USA* 103(20):7829–7834.
15. Hosfield DJ, et al. (2004) Structural basis for bisphosphonate-mediated inhibition of isoprenoid biosynthesis. *J Biol Chem* 279(10):8526–8529.
16. Salcius M, et al. (2014) SEC-TID: A label-free method for small-molecule target identification. *J Biomol Screen*, 10.1177/1087057114522691.
17. Zhang Y, et al. (2009) Lipophilic bisphosphonates as dual farnesyl/geranylgeranyl diphosphate synthase inhibitors: An X-ray and NMR investigation. *J Am Chem Soc* 131(14):5153–5162.
18. Zhang Y, et al. (2010) Lipophilic pyridinium bisphosphonates: Potent gammadelta T cell stimulators. *Angew Chem Int Ed Engl* 49(6):1136–1138.
19. No JH, et al. (2012) Lipophilic analogs of zoledronate and risedronate inhibit *Plasmodium* geranylgeranyl diphosphate synthase (GGPPS) and exhibit potent antimalarial activity. *Proc Natl Acad Sci USA* 109(11):4058–4063.
20. Lindert S, et al. (2013) Farnesyl diphosphate synthase inhibitors from in silico screening. *Chem Biol Drug Des* 81(6):742–748.
21. Liu J, et al. (2014) Syntheses and characterization of non-bisphosphonate quinoline derivatives as new FPPS inhibitors. *Biochim Biophys Acta* 1840(3):1051–1062.
22. Christen M, et al. (2005) The GROMOS software for biomolecular simulation: GROMOS05. *J Comput Chem* 26(16):1719–1751.
23. Schrödinger LLC (2012) *Schrodinger Suite 2012* (Schrödinger, LLC, New York).
24. Trott O, Olson AJ (2010) AutoDock Vina: Improving the speed and accuracy of docking with a new scoring function, efficient optimization, and multithreading. *J Comput Chem* 31(2):455–461.
25. Friesner RA, et al. (2004) Glide: A new approach for rapid, accurate docking and scoring. 1. Method and assessment of docking accuracy. *J Med Chem* 47(7):1739–1749.
26. Friesner RA, et al. (2006) Extra precision glide: Docking and scoring incorporating a model of hydrophobic enclosure for protein-ligand complexes. *J Med Chem* 49(21): 6177–6196.
27. Halgren TA, et al. (2004) Glide: A new approach for rapid, accurate docking and scoring. 2. Enrichment factors in database screening. *J Med Chem* 47(7):1750–1759.
28. Montalvetti A, et al. (2003) Farnesyl pyrophosphate synthase is an essential enzyme in *Trypanosoma brucei*. In vitro RNA interference and in vivo inhibition studies. *J Biol Chem* 278(19):17075–17083.
29. Webb MR (1992) A continuous spectrophotometric assay for inorganic phosphate and for measuring phosphate release kinetics in biological systems. *Proc Natl Acad Sci USA* 89(11):4884–4887.
30. Paris D, et al. (2010) Reduction of beta-amyloid pathology by celastrol in a transgenic mouse model of Alzheimer's disease. *J Neuroinflammation* 7:17.
31. Sha M, et al. (2014) Celastrol induces apoptosis of gastric cancer cells by miR-21 inhibiting PI3K/Akt-NF-κB signaling pathway. *Pharmacology* 93(1-2):39–46.

32. Yang C, et al. (2014) Celastrol increases glucocerebrosidase activity in Gaucher disease by modulating molecular chaperones. *Proc Natl Acad Sci USA* 111(1):249–254.
33. Liu Z, et al. (2014) Cancerous inhibitor of PP2A is targeted by natural compound celastrol for degradation in non-small-cell lung cancer. *Carcinogenesis* 35(4):905–914.
34. Zapata B, et al. (2013) Cytotoxic, immunomodulatory, antimycotic, and antiviral activities of semisynthetic 14-hydroxyabietane derivatives and triptoquinone C-4 epimers. *Med. Chem. Commun.* 4:1239–1246.
35. Burmistrova O, et al. (2013) Antiproliferative activity of abietane diterpenoids against human tumor cells. *J Nat Prod* 76(8):1413–1423.
36. Kuźma L, et al. (2012) Antimicrobial and anti-biofilm properties of new taxodione derivative from hairy roots of *Salvia austriaca*. *Phytomedicine* 19(14):1285–1287.
37. Gordaliza M (2010) Cytotoxic terpene quinones from marine sponges. *Mar Drugs* 8(12):2849–2870.
38. Tada M, Kurabe J, Yoshida T, Ohkanda T, Matsumoto Y (2010) Syntheses and antibacterial activities of diterpene catechol derivatives with abietane, totarane and podocarpane skeletons against methicillin-resistant *Staphylococcus aureus* and *Propionibacterium acnes*. *Chem Pharm Bull (Tokyo)* 58(6):818–824.
39. Zaghloul AM, Gohar AA, Naiem ZA-AM, Abdel Bar FM (2008) Taxodione, a DNA-binding compound from *Taxodium distichum* L. (Rich.). *Z Naturforsch C* 63(5-6): 355–360.
40. Raja SM, et al. (2011) Anticancer activity of Celastrol in combination with ErbB2-targeted therapeutics for treatment of ErbB2-overexpressing breast cancers. *Cancer Biol Ther* 11(2):263–276.
41. Schmitz FJ, Lakshmi V, Powell DR, Van der Helm D (1984) Arenarol and arenarone: Sesquiterpenoids with rearranged drimane skeletons from the marine sponge *Dysidea arenaria*. *J Org Chem* 49(2):241–244.
42. Valdar WS (2002) Scoring residue conservation. *Proteins* 48(2):227–241.
43. Wallace AC, Laskowski RA, Thornton JM (1995) LIGPLOT: A program to generate schematic diagrams of protein-ligand interactions. *Protein Eng* 8(2):127–134.
44. Durrant JD, de Oliveira CA, McCammon JA (2011) POVME: An algorithm for measuring binding-pocket volumes. *J Mol Graph Model* 29(5):773–776.
45. Epand RF, Epand RM, Jung CY (2001) Ligand-modulation of the stability of the glucose transporter GLUT 1. *Protein Sci* 10(7):1363–1369.
46. Cooper A (1992) Effect of cyclodextrins on the thermal stability of globular proteins. *J Am Chem Soc* 114(23):9208–9209.
47. Choi BS, et al. (2014) Celastrol from 'Thunder God Vine' protects SH-SY5Y cells through the preservation of mitochondrial function and inhibition of p38 MAPK in a rotenone model of Parkinson's disease. *Neurochem Res* 39(1):84–96.
48. Sreeramulu S, Gande SL, Göbel M, Schwalbe H (2009) Molecular mechanism of inhibition of the human protein complex Hsp90-Cdc37, a kinome chaperone-cochaperone, by triterpene celastrol. *Angew Chem Int Ed Engl* 48(32):5853–5855.
49. Klaić L, Morimoto RI, Silverman RB (2012) Celastrol analogues as inducers of the heat shock response. Design and synthesis of affinity probes for the identification of protein targets. *ACS Chem Biol* 7(5):928–937.
50. Klaić L, Trippier PC, Mishra RK, Morimoto RI, Silverman RB (2011) Remarkable stereospecific conjugate additions to the Hsp90 inhibitor celastrol. *J Am Chem Soc* 133(49):19634–19637.
51. Hanson RL, Lardy HA, Kupchan SM (1970) Inhibition of phosphofructokinase by quinone methide and alpha-methylene lactone tumor inhibitors. *Science* 168(3929): 378–380.
52. Yang Z, et al. (2001) Synthesis of variously oxidized abietane diterpenes and their antibacterial activities against MRSA and VRE. *Bioorg Med Chem* 9(2):347–356.
53. Case DA, et al. (2005) The Amber biomolecular simulation programs. *J Comput Chem* 26(16):1668–1688.
54. Hornak V, et al. (2006) Comparison of multiple Amber force fields and development of improved protein backbone parameters. *Proteins* 65(3):712–725.
55. Lindorff-Larsen K, et al. (2010) Improved side-chain torsion potentials for the Amber ff99SB protein force field. *Proteins* 78(8):1950–1958.
56. Ryckaert J-P, Ciccotti G, Berendsen HJC (1977) Numerical integration of the cartesian equations of motion of a system with constraints: Molecular dynamics of n-alkanes. *J Comput Phys* 23(3):327–341.
57. Grant BJ, Rodrigues AP, ElSawy KM, McCammon JA, Caves LS (2006) Bio3d: An R package for the comparative analysis of protein structures. *Bioinformatics* 22(21): 2695–2696.
58. Abseher R, Nilges M (1998) Are there non-trivial dynamic cross-correlations in proteins? *J Mol Biol* 279(4):911–920.
59. VanAalten DMF, DeGroot BL, Findlay JBC, Berendsen HJC, Amadei A (1997) A comparison of techniques for calculating protein essential dynamics. *J Comput Chem* 18(2):169–181.
60. Mao J, et al. (2006) Solid-state NMR, crystallographic, and computational investigation of bisphosphonates and farnesyl diphosphate synthase-bisphosphonate complexes. *J Am Chem Soc* 128(45):14485–14497.
61. Mao J, et al. (2004) Crystallization and preliminary X-ray diffraction study of the farnesyl diphosphate synthase from *Trypanosoma brucei*. *Acta Crystallogr D Biol Crystallogr* 60(Pt 10):1863–1866.
62. Zhang Y, et al. (2013) Chemo-immunotherapeutic antimalarials targeting isoprenoid biosynthesis. *ACS Med Chem Lett* 4(4):423–427.
63. Minor W, Cymborowski M, Otwinowski Z, Chruszcz M (2006) HKL-3000: The integration of data reduction and structure solution—from diffraction images to an initial model in minutes. *Acta Crystallogr D Biol Crystallogr* 62(Pt 8):859–866.
64. Winn MD, et al. (2011) Overview of the CCP4 suite and current developments. *Acta Crystallogr D Biol Crystallogr* 67(Pt 4):235–242.
65. Emsley P, Lohkamp B, Scott WG, Cowtan K (2010) Features and development of Coot. *Acta Crystallogr D Biol Crystallogr* 66(Pt 4):486–501.
66. Laskowski RA, Swindells MB (2011) LigPlot+: Multiple ligand-protein interaction diagrams for drug discovery. *J Chem Inf Model* 51(10):2778–2786.
67. Laskowski RA, et al. (1997) PDBsum: A Web-based database of summaries and analyses of all PDB structures. *Trends Biochem Sci* 22(12):488–490.
68. Schrödinger LLC (2013) The PyMOL molecular graphics system (Schrödinger, LLC, New York), Version 1.3.
69. Rieger CE, Lee J, Turnbull JL (1997) A continuous spectrophotometric assay for aspartate transcarbamylase and ATPases. *Anal Biochem* 246(1):86–95.
70. Zhang Y, et al. (2006) Activity of nitrogen-containing and non-nitrogen-containing bisphosphonates on tumor cell lines. *J Med Chem* 49(19):5804–5814.
71. PerkinElmer (2013) ChemDraw (PerkinElmer Informatics), Version 13.0.2.3020. Available at www.cambridgesoft.com/Ensemble_for_Chemistry/ChemDraw/. Accessed May 27, 2014.

SI Appendix

Taxodione and Arenarone Inhibit Farnesyl Diphosphate Synthase by Binding to the Isopentenyl Diphosphate Site

Yi-Liang Liu, Steffen Lindert, Wei Zhu, Ke Wang, J. Andrew McCammon, Eric Oldfield

SI Appendix

SI Materials and Methods

Compounds **9**, **11**, **12** and **13** were obtained from the Drug Synthesis and Chemistry Branch, DTP, Division of Cancer Treatment and Diagnostics, NCI (Bethesda, MD). Compound **10** (NCI-9037) was purchased from Aldrich (Milwaukee, WI). The structures of all compounds investigated were confirmed by using ^{1}H NMR spectroscopy at 400 MHz or 500 MHz on Varian (Palo Alto, CA) Unity spectrometers. The gCOSY and NOESY spectra were obtained at Spectral Data Services, Incorporated, Urbana, Illinois, using an Agilent Inova400. HPLC was performed using an Agilent LC/MSD Trap XCT Plus system (Agilent Technologies, Santa Clara, CA) with a 1100 series HPLC system including a de-gasser, an autosampler, a binary pump, and a multiple-wavelength detector. High-resolution mass spectra were obtained at the University of Illinois Mass Spectrometry Laboratory.

Celastrol (**9**) HRMS (ESI) m/z calcd. for $C_{29}H_{39}O_4$ [M+H$^+$] 451.2848, found 451.2853. 99.5 % pure as determined by analytical HPLC.

Compound **10** (NCI-9037) HRMS (ESI) m/z calcd. for $C_{19}H_{13}O_6$ [M+H$^+$] 337.0712, found 337.0710. 92.4 % pure as determined by analytical HPLC.

Taxodione (**11**) ^{1}H NMR (500 MHz, $CDCl_3$): δ 7.57 (s, 1H), 6.88 (s, 1H), 6.21 (s, 1H), 3.11 - 3.05 (m, 1H), 2.60 (s, 1H), 1.82-1.40 (m, 6H), 1.27 (s, 6H), 1.18 (d, J = 6.5 Hz, 3H), 1.16 (d, J = 6.5 Hz, 3H), 1.12 (s, 3H). HRMS (ESI) m/z calcd. for $C_{20}H_{27}O_3$ [M+H$^+$] 315.1960, found 315.1967. 95.2 % pure as determined by analytical HPLC.

Taxodone (**12**) HRMS (ESI) m/z calcd. for $C_{20}H_{29}O_3$ [M+H$^+$] 317.2117, found 317.2118. 92.2 % pure as determined by analytical HPLC.

Arenarone (**13**) HRMS (ESI) m/z calcd. for $C_{21}H_{29}O_2$ [M+H$^+$] 313.2168, found 313.2167. 98.9 % pure as determined by analytical HPLC.

Analyzed data are compiled in Fig. S9.

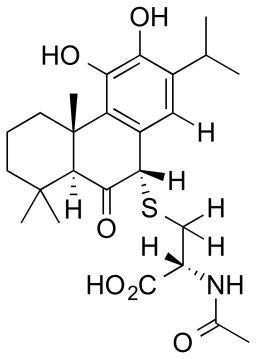

17

N-acetyl-S-((4a*S*,9*S*,10a*S*)-5,6-dihydroxy-7-isopropyl-1,1,4a-trimethyl-10-oxo-1, 2, 3, 4, 4a, 9, 10, 10a- octahydrophen- anthren-9-yl)-L-cysteine (compound **17**)

To a solution of taxodione (**11**) (1.4 mg, 0.0044 mmol) in CD_3OD (0.3 mL) was added N-acetylcysteine (0.76 mg, 0.0046 mmol) in CD_3OD (0.3 mL), and the reaction was stirred for 4 hrs at 37 ˚C. The product was analyzed without further purification. ^1H NMR (400 MHz, CD_3OD): δ 6.74 (s, 1H), 4.87 - 4.81 (m, 1H), 4.11 (s, 1H), 3.41 (s, 1H), 3.21 – 3.14 (m, 2H), 2.73 – 2.65 (m, 1H), 2.08 (s, 3H), 1.80 - 1.72 (m, 2H), 1.58-1.53(m, 2H), 1.40 (s, 3H), 1.39 -1.34 (m, 2H), 1.25 (s, 3H), 1.21 (d, J = 7.0 Hz, 3H), 1.18 (d, J = 7.0 Hz, 3H), 1.04 (s, 3H). HRMS (ESI) m/z calcd. for $C_{25}H_{36}NO_6S$ $[M+H^+]$ 478.2263, found 478.2243.

Table S1. HsFPPS, TbFPPS, HsGGPPS and MCF-7 tumor cell inhibition (IC_{50} values in µM).

	ID	HsFPPS (PPi assay)	TbFPPS (PPi assay)	HsGGPPS (radio assay)	MCF-7 (MTT assay)
Celastrol	**9**	>200	17.1	31.9	0.2
NSC9037	**10**	81.0	54.2	>200	[a]N.D.
Taxodione	**11**	1.2	17.3	19.8	2.0
Taxodone	**12**	2.4	43.1	46.3	[a]N.D
Arenarone	**13**	1.1	27.8	21.2	17.1

[a]N.D.: not determined.

Table S2. Pocket-volume results.

PDB ID code	Volume ($Å^3$)	Conformation	Ligand
4H5D	445	closed	bisphosphonate (YS0470)
2F8C	453	closed	bisphosphonate (zoledronate), PPi
4H5E	455	closed	bisphosphonate (YS0470), IPP
1ZW5	462	closed	bisphosphonate (zoledronate), IPP
2F89	462	closed	bisphosphonate (pamidronate)
2F94	466	closed	bisphosphonate (ibandronate)
4GA3	467	closed	bisphosphonate (BPH-1260)
2F8Z	469	closed	bisphosphonate (zoledronate), IPP
3N46	472	closed	bisphosphonate (zoledronate), Novartis inhibitor (NOV_980)
4P0W	472	closed	bisphosphonate (zoledronate), Arenarone
2F9K	473	closed	bisphosphonate (zoledronate)
2F92	482	closed	bisphosphonate (alendronate)
2VF6	485	closed	bisphosphonate (minodronate)
4L2X	488	closed	bisphosphonate (CL02134)
1YV5	501	closed	bisphosphonate (risedronate)
2OPM	506	closed	bisphosphonate (BPH-461)
3B7L	508	closed	bisphosphonate (minodronate)
1YQ7	512	closed	bisphosphonate (risedronate)
4P0V	512	closed	bisphosphonate (zoledronate), Taxodione
3N45	516	closed	bisphosphonate (zoledronate), Novartis inhibitor (FBS_04)
3S4J	531	closed	bisphosphonate (risedronate)
3RYE	536	closed	bisphosphonate
2QIS	537	closed	bisphosphonate (risedronate)
4H5C	550	closed	bisphosphonate (YS0470), Pi
4DEM	557	closed	bisphosphonate (YS_04_70)
2RAH	582	closed	bisphosphonate
3CP6	601	closed	bisphosphonate
2OPN	607	closed	bisphosphonate (BPH-527)
4JVJ	626	closed	bisphosphonate (CL01131)
Avg, closed	508±50		
2F7M	817	open	apo (unliganded)
3N5J	830	open	Novartis inhibitor (NOV_311)
4P0X	845	open	Taxodione
3N5H	847	open	Novartis inhibitor (NOV_304)
3N1V	852	open	Novartis inhibitor (FBS_01)
3N3L	859	open	Novartis inhibitor (FBS_03)
3N6K	870	open	Novartis inhibitor (NOV_823)
3N1W	878	open	Novartis inhibitor (FBS_02)
3N49	886	open	Novartis inhibitor (NOV_292)
1FPS	893	open	apo (unliganded)
Avg, open	858±24		

Fig. S1. Structures of the 50 compounds obtained from the NCI/DTP collection that were screened for inhibition of HsFPPS and TbFPPS. The numbers shown are NSC (NIH/DTP) code numbers initially.

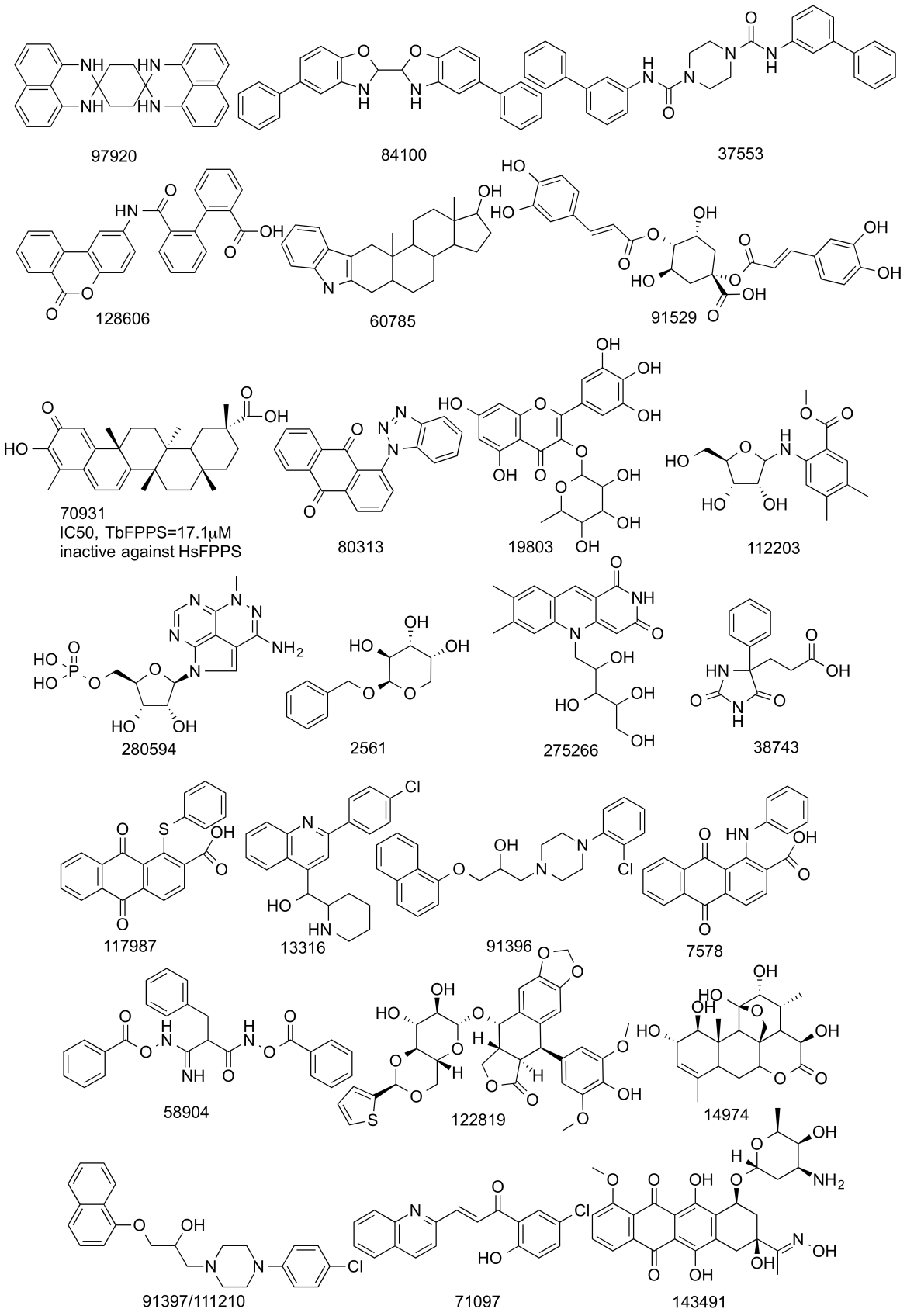

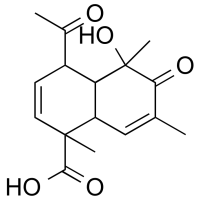

49643

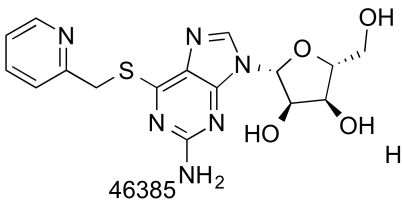

46385

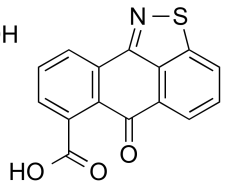

39938

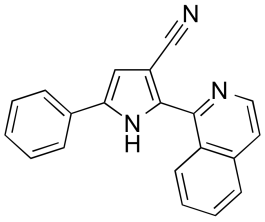

116640

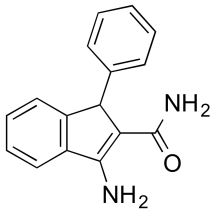

108750

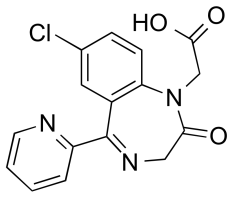

157725

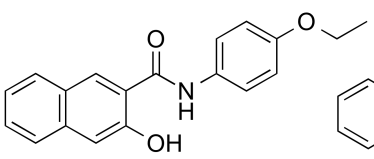

50690

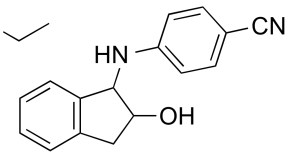

69421

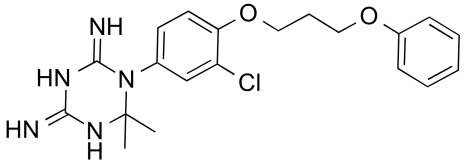

133071

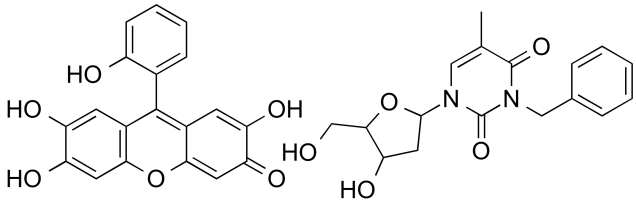

9037

IC50, HsFPPS=81μM

IC50,TbFPPS=54μM

106464

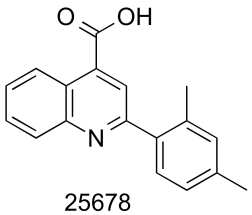

25678

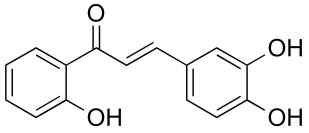

37433

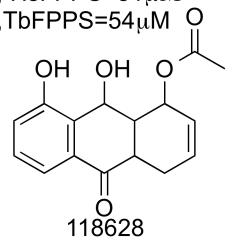

118628

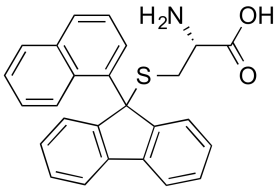

123527

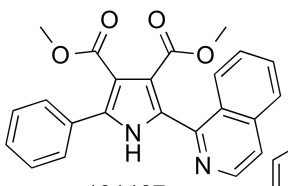

131467

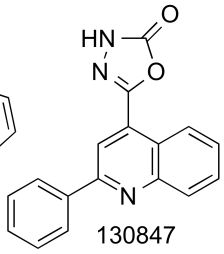

130847

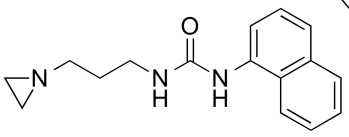

101298

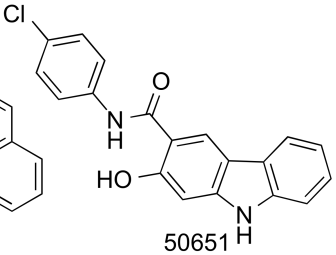

50651

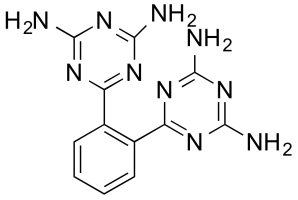

4429

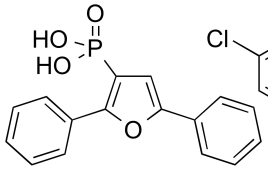

43344

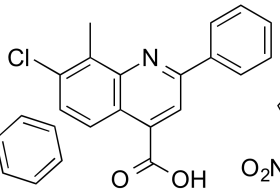

40306

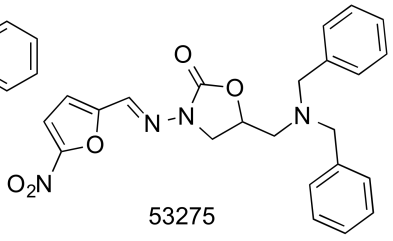

53275

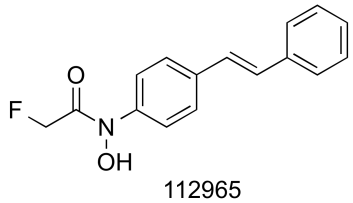

112965

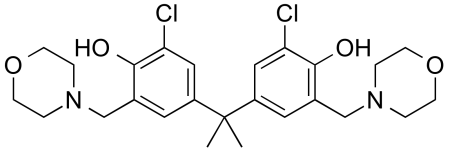

64876

Fig. S2. Structures of the 25 compounds from the first similarity search (on **9**) tested against HsFPPS and TbFPPS. The numbers shown are NSC (NIH/DTP) code numbers.

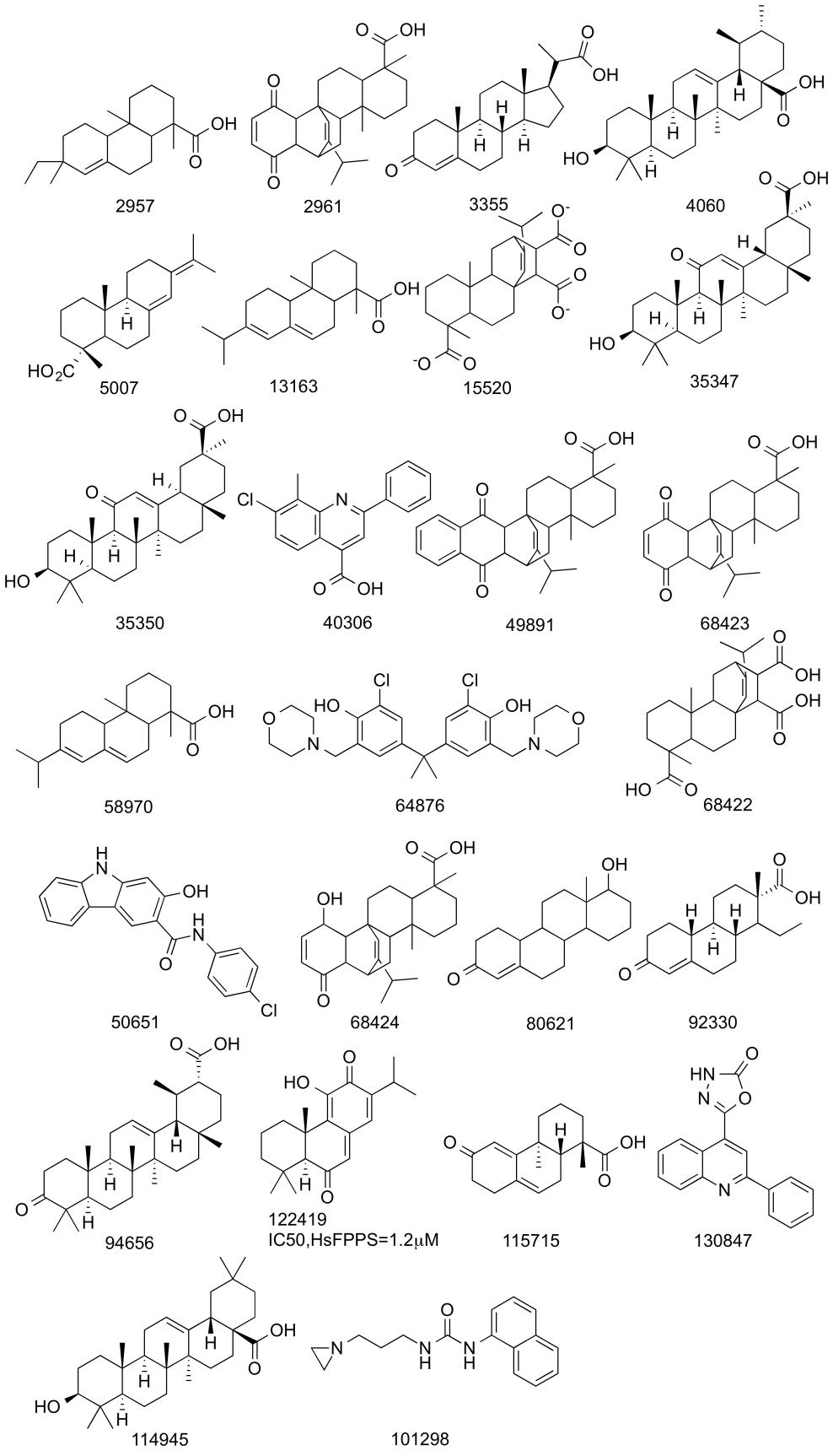

Fig. S3. Structures of the 15 compounds based on a similarity search (on **11**), tested against HsFPPS. NSC122420 (**12**) is taxodone; NSC 613794 is arenarone (**13**).

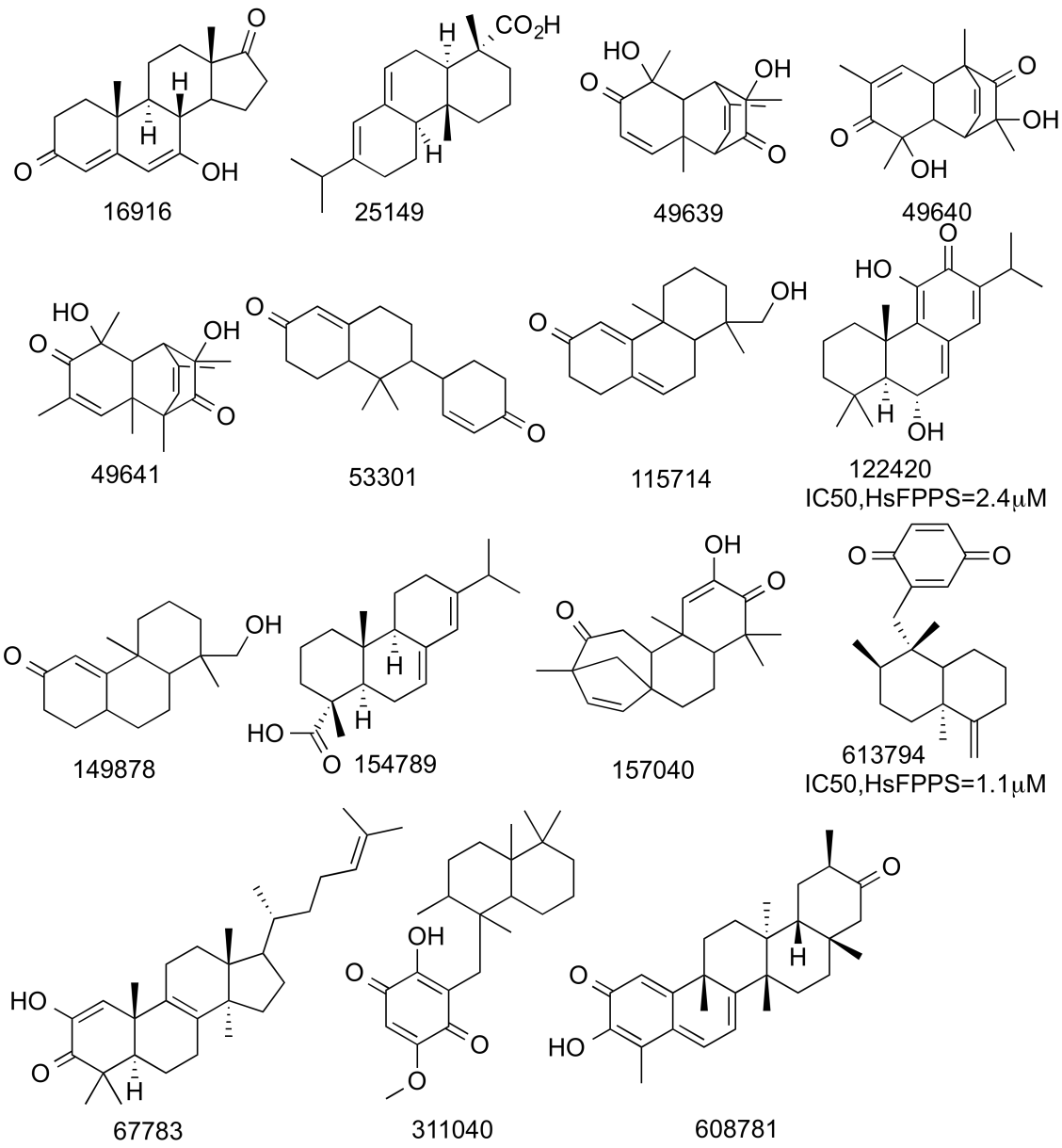

Fig. S4. 2Fo-Fc map of ligands calculated at 1.0σ. (A) Taxodione+zoledronate (PDB ID 4P0V). (B) Taxodione (2 molecules; PDB ID 4P0X). (C) Arenarone+zoledronate (PDB ID 4P0W).

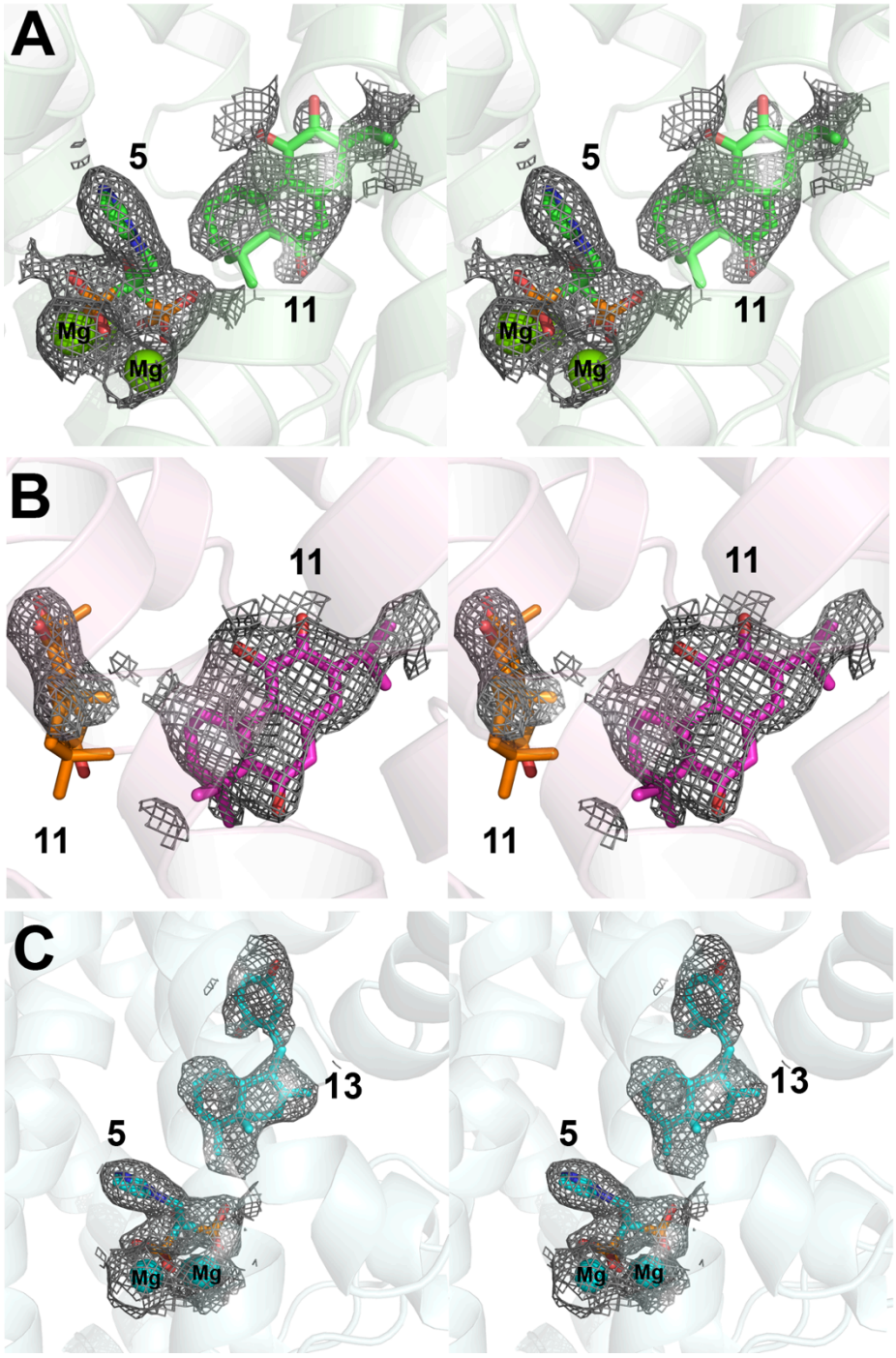

Fig. S5. Protein-ligand interactions in taxodione+zoledronate HsFPPS structure (PDB ID 4P0V).

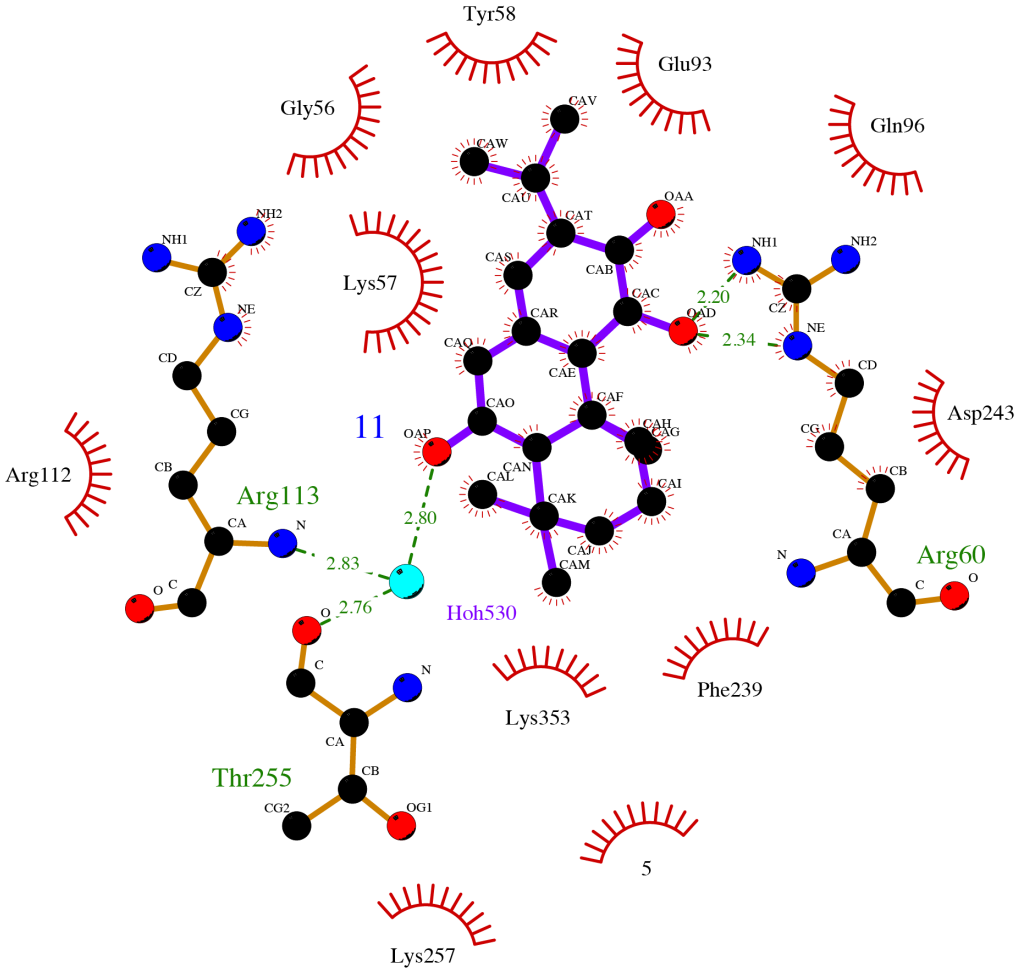

Fig. S6. Protein-ligand (and ligand-solvent) interactions in the taxodione structure (PDB ID 4P0X). (A) One ligand binds in the IPP site. (B) One ligand is solvent accessible.

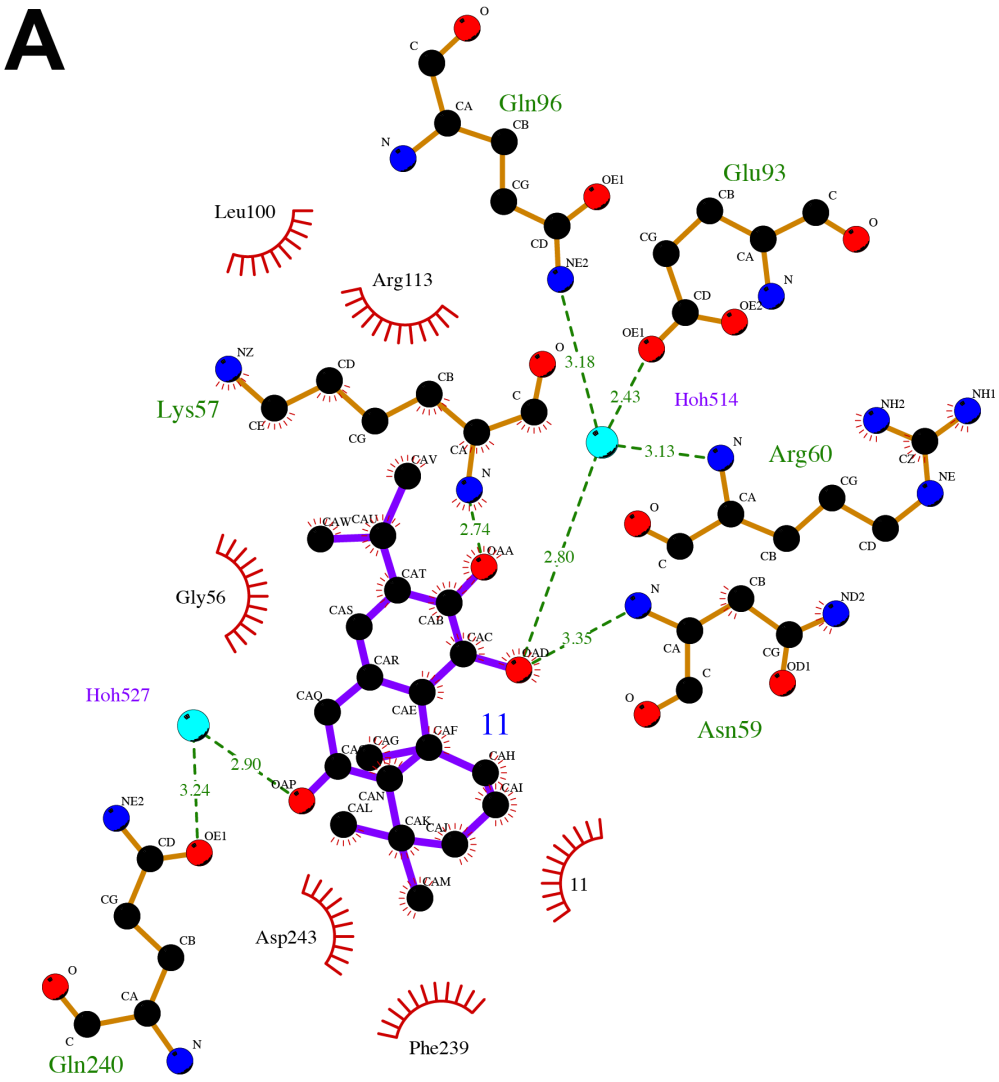

Fig. S7. Ligand-protein interactions in the arenarone+zoledronate HsFPPS structure (PDB ID 4P0W).

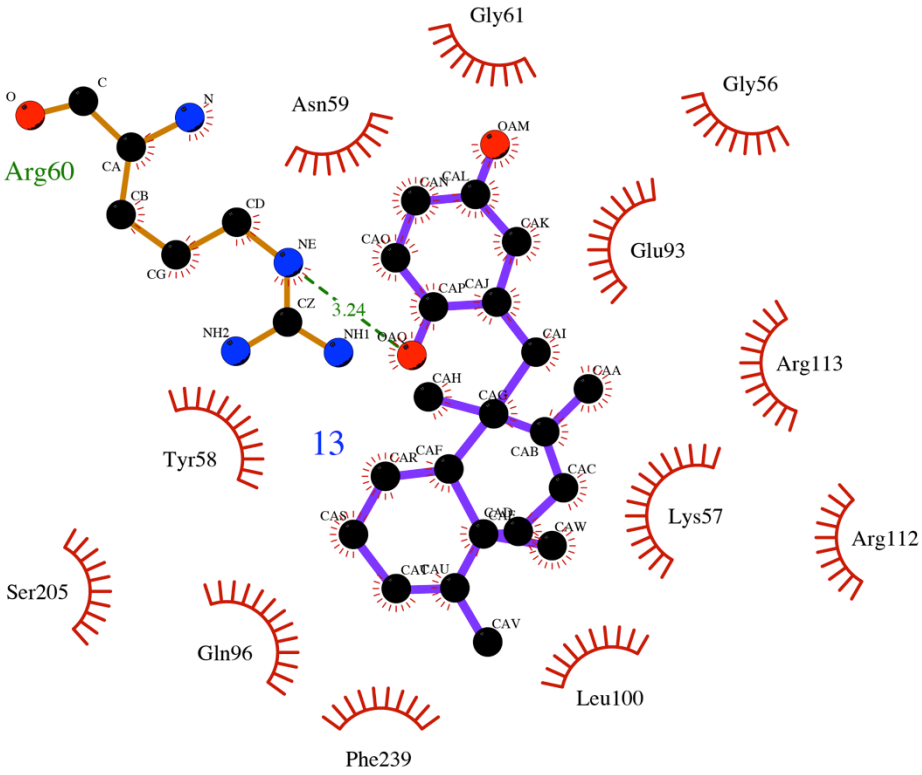

Fig. S8. High resolution mass spectrometry and NMR data for **17**.

A

Elemental Composition Report **Page 1**

Single Mass Analysis
Tolerance = 10.0 PPM / DBE: min = -1.5, max = 600.0
Element prediction: Off
Number of isotope peaks used for i-FIT = 3

Monoisotopic Mass, Even Electron Ions
45 formula(e) evaluated with 1 results within limits (all results (up to 1000) for each mass)
Elements Used:
C: 0-125 H: 0-250 N: 1-3 O: 5-7 S: 1-1

wang, ke ¬, W-14-04 University of Illinois, SCS, Mass Spectrometry Lab Q-tof UE521
Qtof_50983 30 (2.246) AM (Cen,3, 80.00, Ar,15000.0,716.46,0.70,LS 3); Sm (SG, 2x3.00); Cm (30:33) 1: TOF MS ES+
2.91e+002

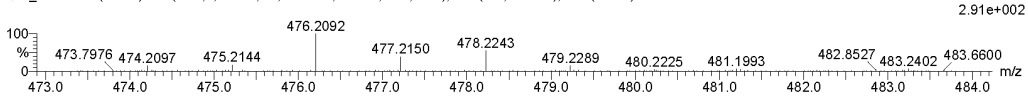

Minimum:		5.0	10.0	-1.5		
Maximum:				600.0		
Mass	Calc. Mass	mDa	PPM	DBE	i-FIT	Formula
478.2243	478.2263	-2.0	-4.2	8.5	0.2	C25 H36 N O6 S

B

^{1}H NMR: **11** + N-acetylcysteine in CD_3OD at 37 ˚C (4 hrs)

17

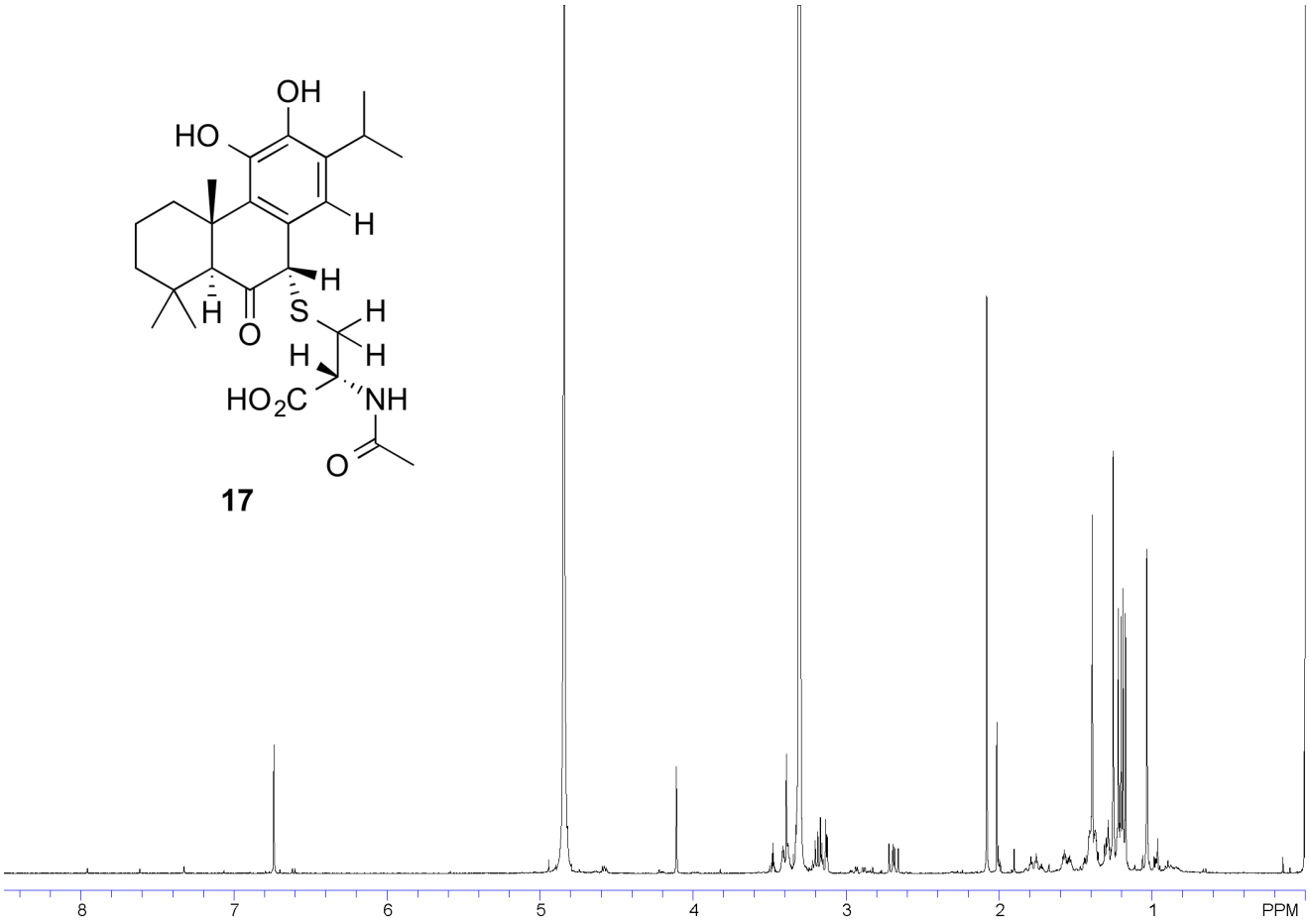

20140305, CD3OD, 1H, 400MHz USER: TT -- DATE: Mar 5 2014

F1: 399.622	F2: 100.493	SW1: 7023		OF1: 3122.9		PTS1d: 17500 , 32768
EX: s2pul		PW: 6.0 us	PD: 5.0 sec	NA: 128	LB: 0.2	Nuts - $ericz14.001.fid

C

gCOSY: **11** + N-acetylcysteine in CD_3OD at 37 ˚C (4 hrs)

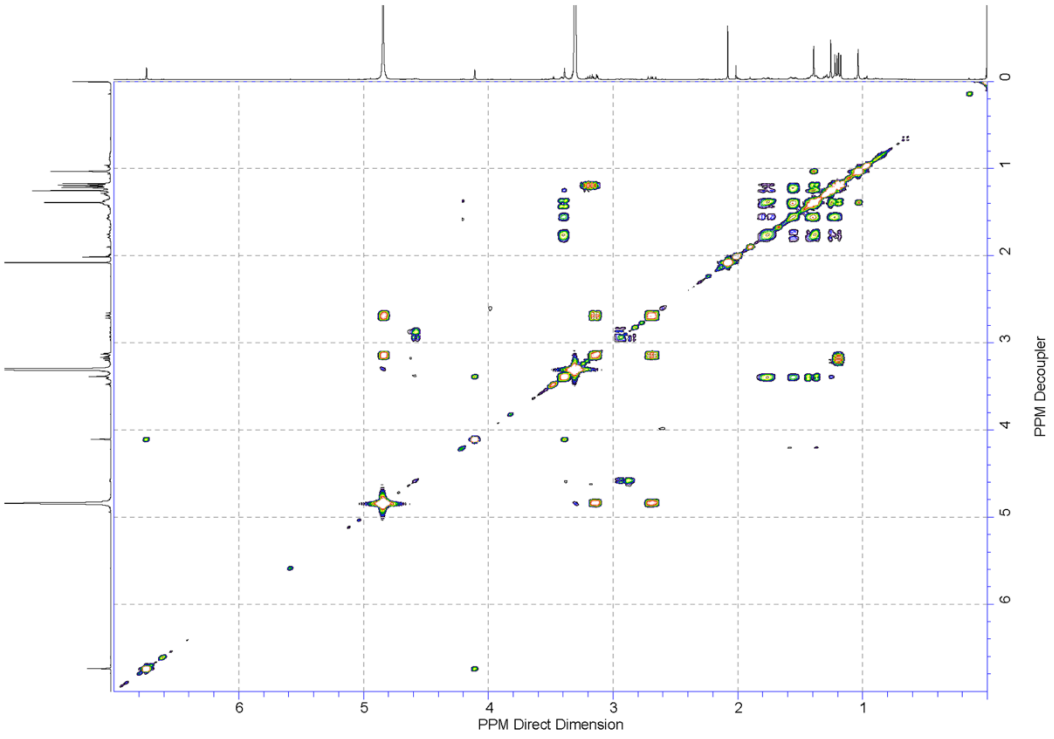

20140305, CD3OD, 1H/1H - COSY, 400MHz						USER: TT -- DATE: Mar 5 2014	
F1: 399.621	F2: 399.621	SW1: 3511	SW2: 3511	OF1: 1419.2	OF2: 1419.2	PTS1d: 525 , 1024	PTS2d: 512 , 1024
EX: gCOSY		PW: 13.6 us	PD: 2.0 sec	NA: 8	LB: 0.0		Nuts - $ericz14.dat01.fid

D

NOESY: **11** + N-acetylcysteine in CD_3OD at 37 ˚C (4 hrs)

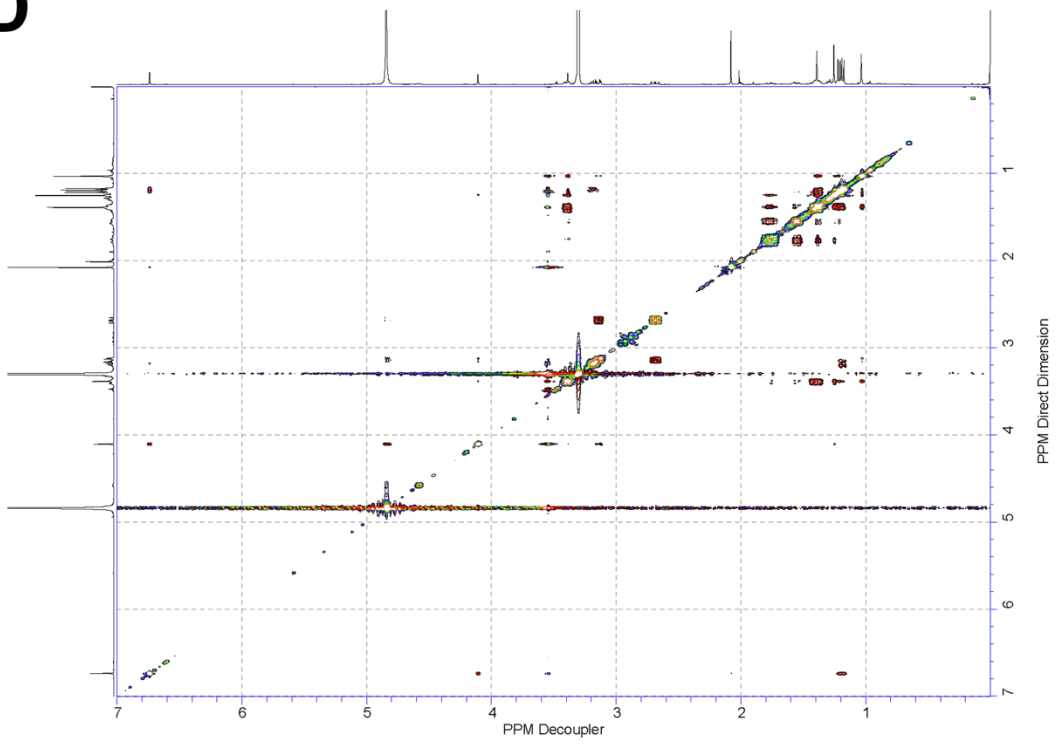

20140305, CD3OD, 1H/1H - NOESY, 400MHz						USER: TT -- DATE: Mar 5 2014	
F1: 399.621	F2: 399.621	SW1: 3511	SW2: 3511	OF1: 1419.6	OF2: 1419.6	PTS1d: 530 , 1024	PTS2d: 512 , 1024
EX: NOESY		PW: 13.6 us	PD: 1.0 sec	NA: 16	LB: 0.0		Nuts - $ericz14.dat02.fid

Fig. S9. ESI-MS of HsFPPS (100 μM) with 100 μM inhibitor. (A) HsFPPS. (B) HsFPPS+Taxodione (**11**). (C) HsFPPS+Celastrol (**9**).

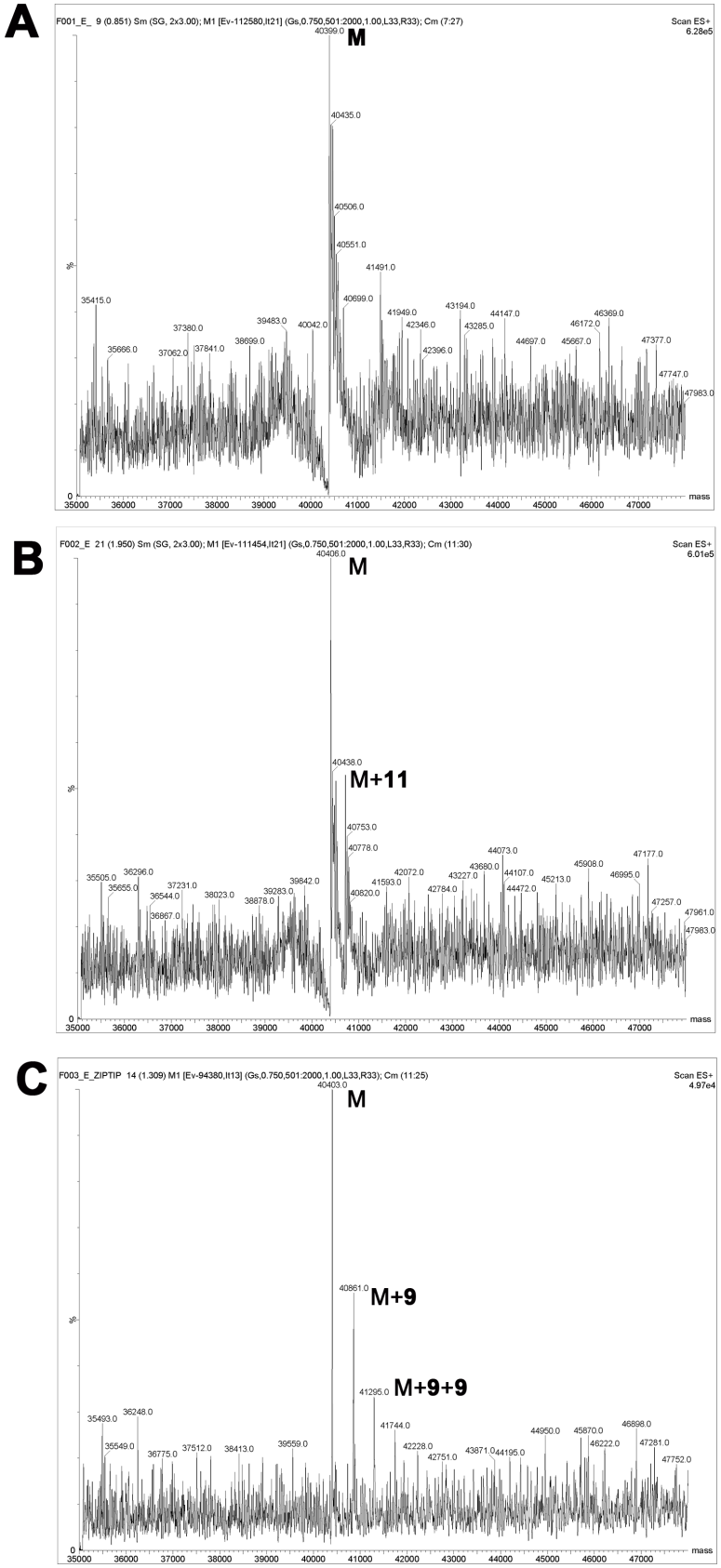

Fig. S10. Analytical HPLC results.

HPLC(UV)/MS analysis of Celastrol (**9**)

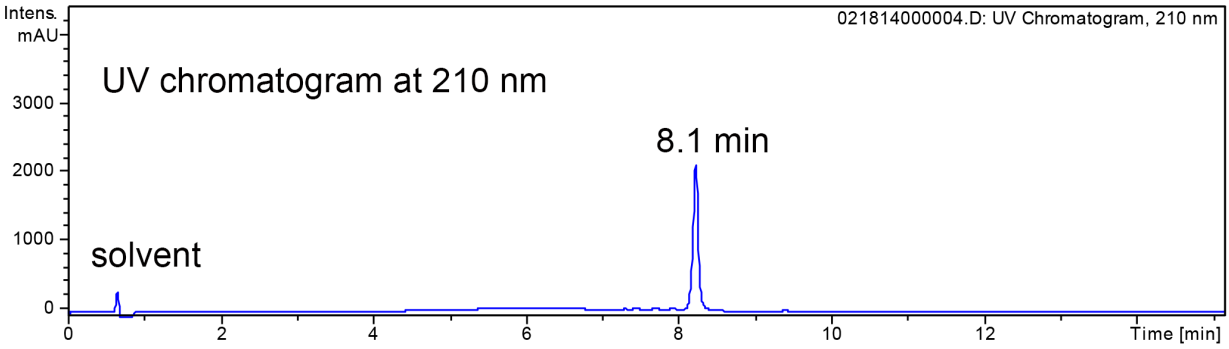

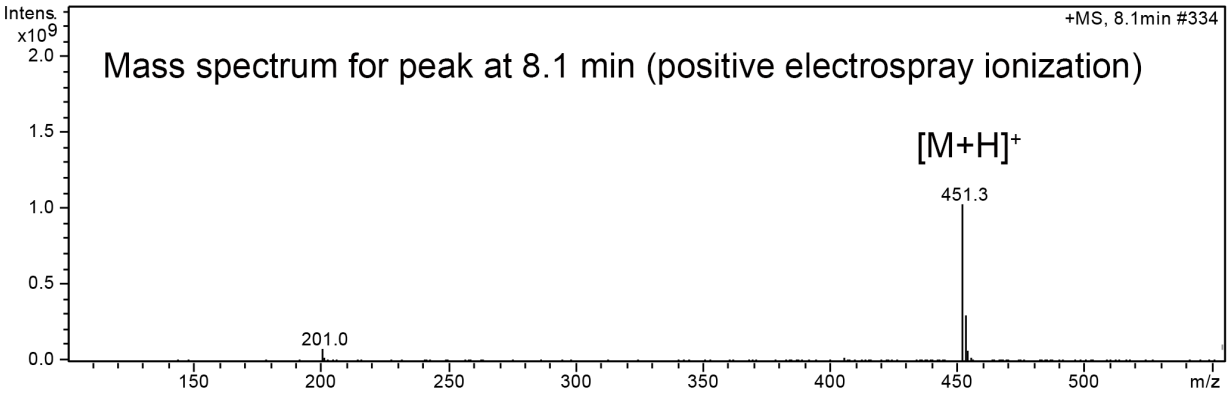

Peak percentage of 8.1 min is 99.5 %.

HRMS report of Celastrol (**9**)

Elemental Composition Report **Page 1**

Single Mass Analysis
Tolerance = 10.0 PPM / DBE: min = -1.5, max = 600.0
Element prediction: Off
Number of isotope peaks used for i-FIT = 3

Monoisotopic Mass, Even Electron Ions
454 formula(e) evaluated with 6 results within limits (all results (up to 1000) for each mass)
Elements Used:
C: 0-125 H: 0-250 N: 0-5 O: 0-6 Na: 0-1

wang, ke, W-14-L4 University of Illinois, SCS, Mass Spectrometry Lab Q-tof UE521
Qtof_51034 35 (2.619) AM (Cen,5, 80.00, Ar,15000.0,716.46,0.70,LS 3); Sm (SG, 2x7.00); Cm (35:36) 1: TOF MS ES+
1.44e+003

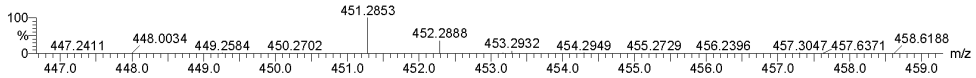

Minimum:				-1.5		
Maximum:		5.0	10.0	600.0		
Mass	Calc. Mass	mDa	PPM	DBE	i-FIT	Formula
451.2853	451.2848	0.5	1.1	10.5	1.4	C29 H39 O4
	451.2862	-0.9	-2.0	15.5	0.7	C30 H35 N4
	451.2838	1.5	3.3	12.5	3.0	C28 H36 N4 Na
	451.2824	2.9	6.4	7.5	5.3	C27 H40 O4 Na
	451.2896	-4.3	-9.5	3.5	22.8	C21 H40 N4 O5 Na
	451.2808	4.5	10.0	6.5	11.5	C24 H39 N2 O6

HPLC(UV)/MS analysis of compound 10 (NCI-9037)

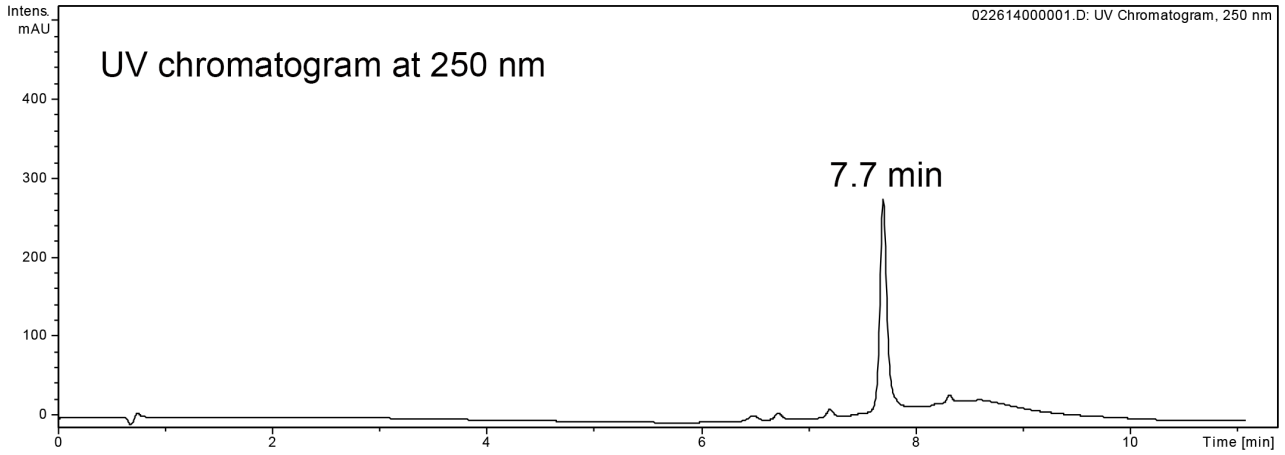

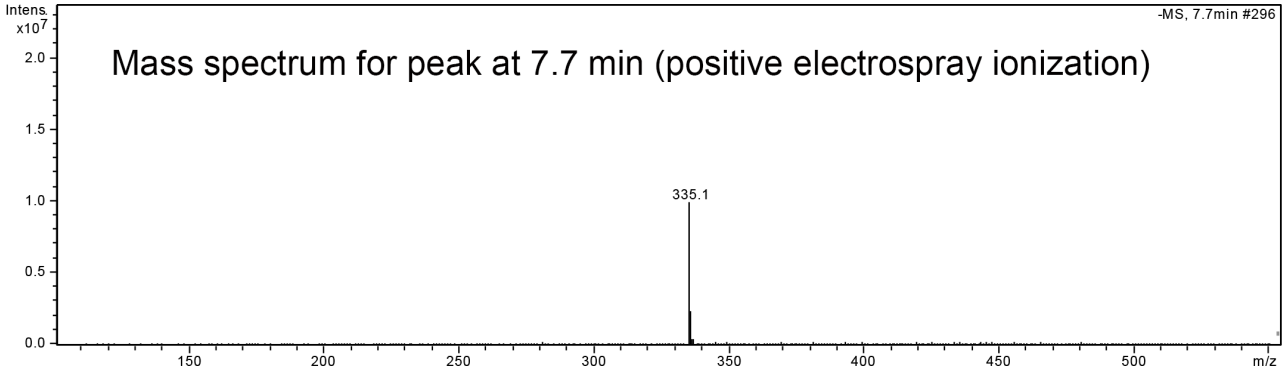

Peak percentage of 7.7 min is 92.4 %.

HRMS report of compound **10** (NCI-9037)

Elemental Composition Report **Page 1**

Single Mass Analysis
Tolerance = 10.0 PPM / DBE: min = -1.5, max = 600.0
Element prediction: Off
Number of isotope peaks used for i-FIT = 3

Monoisotopic Mass, Even Electron Ions
179 formula(e) evaluated with 2 results within limits (all results (up to 1000) for each mass)
Elements Used:
C: 0-125 H: 0-250 N: 0-5 O: 0-6

wang, ke, W-14-L1 University of Illnois, SCS, Mass Spectrometry Lab Q-tof UE521
Qtof_51031a 32 (2.395) AM (Cen,5, 80.00, Ar,15000.0,716.46,0.70,LS 3); Sm (SG, 2x7.00); Cm (29:32) 1: TOF MS ES+
9.15e+002

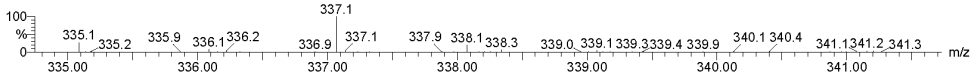

Minimum:				-1.5		
Maximum:		5.0	10.0	600.0		
Mass	Calc. Mass	mDa	PPM	DBE	i-FIT	Formula
337.0710	337.0712	-0.2	-0.6	13.5	2.5	C19 H13 O6
	337.0726	-1.6	-4.7	18.5	6.1	C20 H9 N4 O2

HPLC(UV)/MS analysis of Taxodione (**11**)

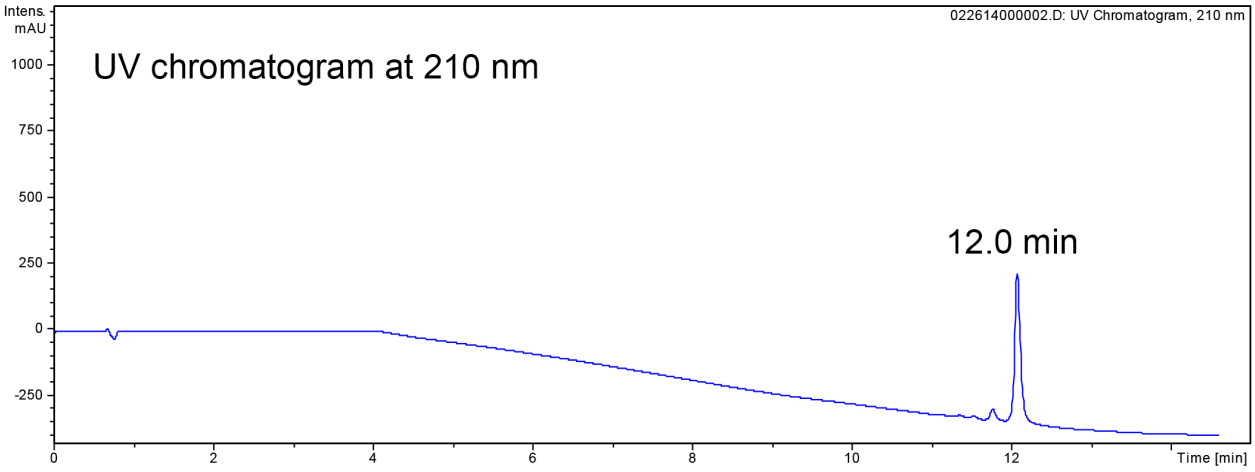

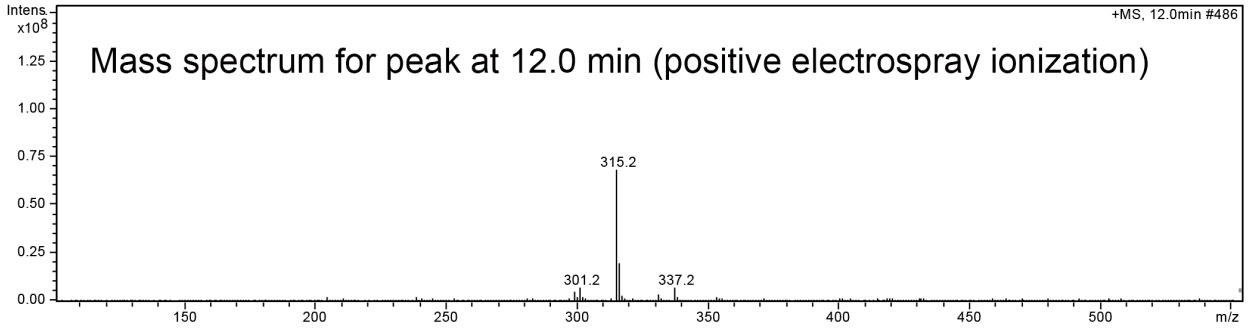

Peak percentage of 12.0 min is 95.2 %.

HRMS report of Taxodione (11)

Elemental Composition Report **Page 1**

Single Mass Analysis
Tolerance = 10.0 PPM / DBE: min = -1.5, max = 600.0
Element prediction: Off
Number of isotope peaks used for i-FIT = 3

Monoisotopic Mass, Even Electron Ions
317 formula(e) evaluated with 2 results within limits (all results (up to 1000) for each mass)
Elements Used:
C: 0-125 H: 0-250 N: 0-5 O: 0-6 Na: 0-1

wang, ke, W-14-L5 University of Illinois, SCS, Mass Spectrometry Lab Q-tof UE521
Qtof_51035 31 (2.321) AM (Cen,5, 80.00, Ar,15000.0,716.46,0.70,LS 3); Sm (SG, 2x7.00); Cm (29:38-3:10x8.000) 1: TOF MS ES+
6.94e+002

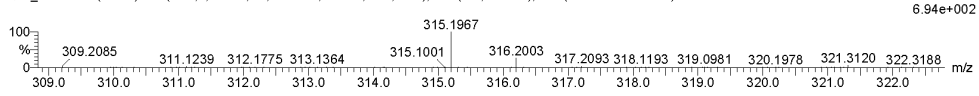

Minimum:			-1.5			
Maximum:		5.0	10.0	600.0		
Mass	Calc. Mass	mDa	PPM	DBE	i-FIT	Formula
315.1967	315.1960	0.7	2.2	7.5	1.8	C20 H27 O3
	315.1936	3.1	9.8	4.5	5.0	C18 H28 O3 Na

HPLC(UV)/MS analysis of Taxodone (**12**)

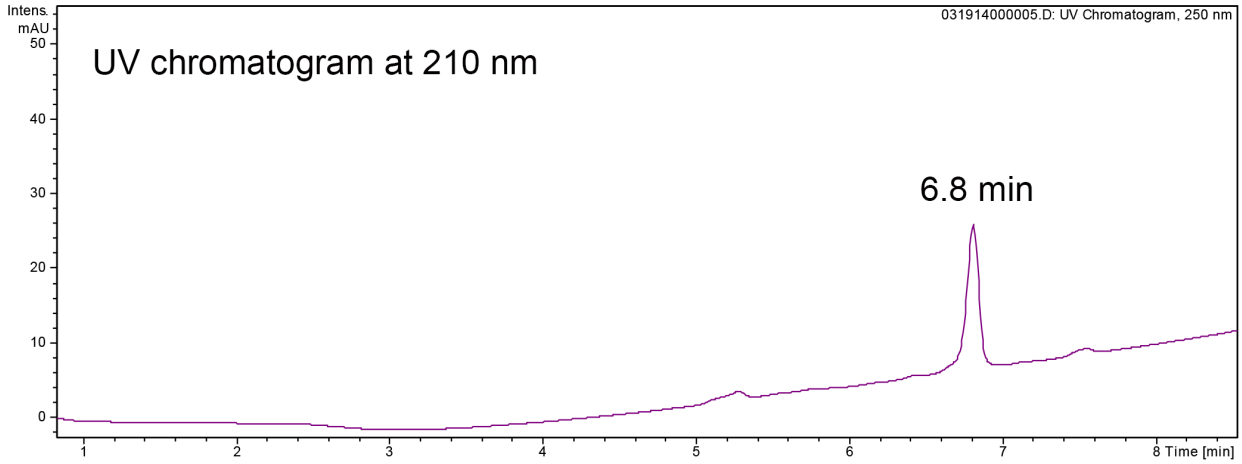

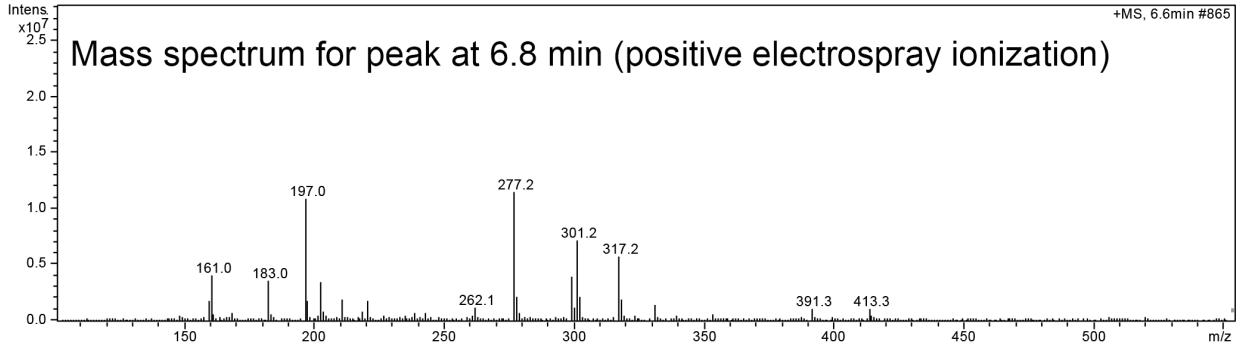

Peak percentage of 6.8 min is 91.6 %.

HRMS report of Taxodone (**12**)

Elemental Composition Report **Page 1**

Single Mass Analysis
Tolerance = 10.0 PPM / DBE: min = -1.5, max = 600.0
Element prediction: Off
Number of isotope peaks used for i-FIT = 3

Monoisotopic Mass, Even Electron Ions
29 formula(e) evaluated with 1 results within limits (all results (up to 1000) for each mass)
Elements Used:
C: 0-125 H: 0-250 O: 0-6

wang, ke, W-14-L2_NaCl — University of Illinois, SCS, Mass Spectrometry Lab — Q-tof UE521
Qtof_51032b 30 (2.246) AM (Cen,5, 80.00, Ar,15000.0,716.46,0.70,LS 3); Sm (SG, 2x7.00); Cm (29:30) — 1: TOF MS ES+ 2.56e+002

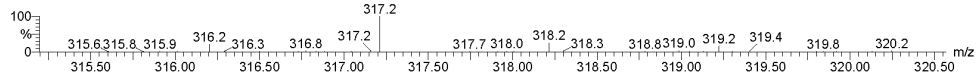

Minimum:				-1.5		
Maximum:		5.0	10.0	600.0		
Mass	Calc. Mass	mDa	PPM	DBE	i-FIT	Formula
317.2118	317.2117	0.1	0.3	6.5	13.7	C20 H29 O3

HPLC(UV)/MS analysis of Arenarone (**13**)

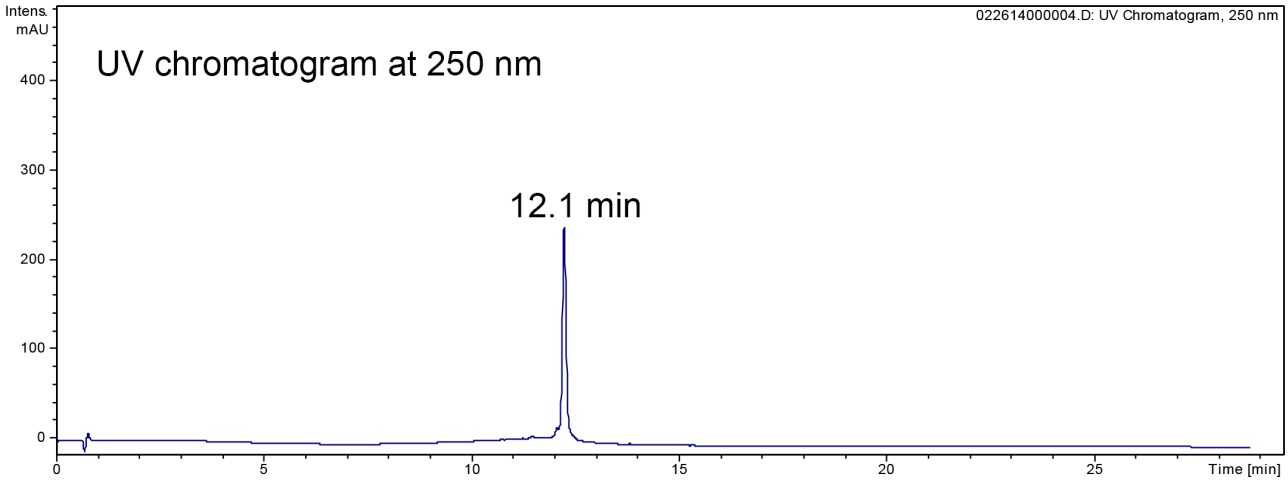

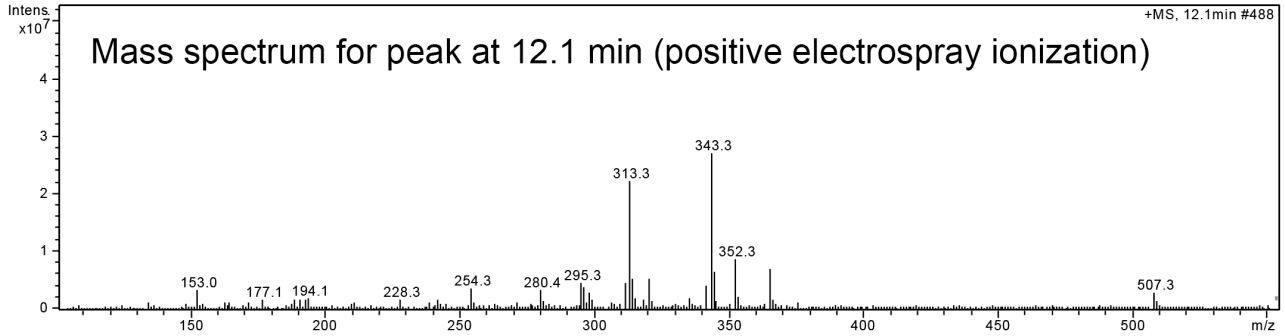

Peak percentage of 12.1 min is 98.9 %.

HRMS report of Arenarone (**13**)

Elemental Composition Report **Page 1**

Single Mass Analysis
Tolerance = 10.0 PPM / DBE: min = -1.5, max = 600.0
Element prediction: Off
Number of isotope peaks used for i-FIT = 3

Monoisotopic Mass, Even Electron Ions
167 formula(e) evaluated with 1 results within limits (all results (up to 1000) for each mass)
Elements Used:
C: 0-125 H: 0-250 N: 0-5 O: 0-6

wang, ke, W-14-L3 University of Illinois, SCS, Mass Spectrometry Lab Q-tof UE521
Qtof_51033a 30 (2.246) AM (Cen,5, 80.00, Ar,15000.0,716.46,0.70,LS 3); Sm (SG, 2x7.00); Cm (29:38-5:9x8.000) 1: TOF MS ES+
6.11e+002

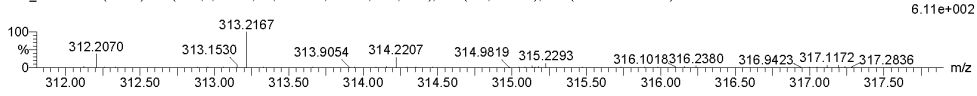

Minimum:				-1.5		
Maximum:		5.0	10.0	600.0		
Mass	Calc. Mass	mDa	PPM	DBE	i-FIT	Formula
313.2167	313.2168	-0.1	-0.3	7.5	22.1	C21 H29 O2